

Nonlinear Evolution of a Baroclinic Wave and Imbalanced Dissipation

Balasubramanya T. Nadiga¹†

Los Alamos National Laboratory, MS-B214, Los Alamos, NM 87545, USA

(Received 7 September 2013)

We consider nonlinear evolution of an unstable baroclinic wave in a regime of rotating stratified flow that is of relevance to *interior* circulation in the oceans and in the atmosphere—a regime characterized by small large-scale Rossby and Froude numbers, a small vertical to horizontal aspect ratio, and no bounding horizontal surfaces. Using high-resolution simulations of the non-hydrostatic Boussinesq equations and companion integrations of the balanced quasi-geostrophic equations, we present evidence for a local route to dissipation of balanced energy directly through interior turbulent cascades. That is, analysis of simulations presented in this study suggest that a developing baroclinic instability can lead to secondary instabilities that can cascade a small fraction of the energy forward to unbalanced scales whereas the bulk of the energy is confined to large balanced scales.

Mesoscale shear and strain resulting from the hydrostatic geostrophic baroclinic instability drive frontogenesis. The fronts in turn support ageostrophic secondary circulation and instabilities. These two processes acting together lead to a quick rise in dissipation rate which then reaches a peak and begins to fall slowly when frontogenesis slows down; eventually balanced and imbalanced modes decouple.

A measurement of the dissipation of balanced energy by imbalanced processes reveals that it scales exponentially with Rossby number of the base flow. We expect that this scaling will hold more generally than for the specific setup we consider given the fundamental nature of the dynamics involved.

In other results, a) A break is seen in the total energy spectrum at small scales: While a steep k^{-3} geostrophic scaling (where k is the three-dimensional wavenumber) is seen at intermediate scales, the smaller scales display a shallower $k^{-5/3}$ scaling, reminiscent of the atmospheric spectra of Nastrom & Gage and b) At the higher of the Rossby numbers considered a minimum is seen in the vertical shear spectrum, reminiscent of similar spectra obtained using in-situ measurements.

1. Introduction

Ocean circulation is mainly forced at large scales and instabilities of the resulting large-scale circulation at scales related to the internal Rossby radius of deformation give rise to intermediate-scale mesoscale eddies (e.g., see Vallis 2006; McWilliams 2006; Gill 1982). The large-scale circulation and mesoscale eddies are however in approximate geostrophic and hydrostatic momentum balance. In this setting, classical geostrophic turbulence theory suggests that such balanced dynamics leads to quasi-two-dimensional behavior at the mesoscales and larger scales (Charney 1971). An expected consequence of the quasi-two-dimensional behavior is an inverse cascade of energy, wherein baroclinic instability injects energy into the barotropic mode and nonlinear barotropic interactions

† Email address for correspondence: balu@lanl.gov

transfer barotropic (kinetic) energy to larger scales. Although the strength, extent, and nature of the barotropic inverse cascade itself is an area of ongoing research (e.g., see Straub & Nadiga 2014, and references therein), an established consequence of balanced turbulence is a confinement of energy to large and intermediate scales. A side effect of such confinement is to render small scale dissipation ineffective in directly dissipating balanced mesoscale and large-scale energy (Charney 1971, and the extensive literature on geostrophic turbulence) Thus a fundamental question regarding the energetics of ocean circulation is as to how the ocean equilibrates in the presence of continuous large-scale forcing and a tendency to confine energy to large and intermediate scales.

The tendency of large-scale quasi-two dimensional (anisotropic) rotating, stratified turbulence to confine energy to the large and intermediate scales is in contrast to the forward energy cascade of small-scale, three dimensional, isotropic turbulence (e.g., see Frisch 1995; Lesieur 1997). Here, by large-scales we mean the range of scales down from the size of the domain to the first internal Rossby radius of deformation. Elsewhere, we also refer to scales of the order of the deformation radius as intermediate scales. The scales and phenomena that span these two asymptotic regimes of turbulence and the interactions of the large-scale flow with boundaries are then expected to hold the answer to the ocean-equilibration question above. The range of such processes include submesoscale and inertia-gravity wave processes and they are further broadly categorized into boundary and surface related processes, inertia-gravity wave processes, and other instability processes (e.g., see Molemaker *et al.* 2005). A large body of recent research has focused on surface related processes in this context. It is beyond the scope of the present article to review this evolving field of research, and the reader is referred to, e.g., McWilliams *et al.* (1998); Molemaker *et al.* (2005); Thomas *et al.* (2008); Molemaker *et al.* (2010); Thomas *et al.* (2013) and references therein. However, it is worth noting that there are a set of fluid dynamical instabilities that underlie this line of research (e.g., see McWilliams *et al.* 1998).

Given that the atmospheric forcing of ocean circulation is mediated by the top surface of the ocean, the importance of understanding the dynamics of this region cannot be over-stated. However, and in part for the same reason, the top surface is a preferred site for a wide range of phenomena including, of course, thermal and momentum exchange with the atmosphere. This leads to surface dynamics being complicated. This renders the surface layer to not be the ideal setting to study the instabilities that underlie balanced-unbalanced interactions.

The aim of this article is two-fold. First, we propose and use an idealized setup devoid of free surfaces—a periodic domain—to study instabilities relevant for balanced-unbalanced interactions. Like in the Charney model of baroclinic instability, baroclinic instability in the setup we consider is due to interior gradients of potential vorticity. In that sense the present setup is a version of the Charney model where the base state is periodic (and presently $\beta = 0$). Equivalently, the setup may be thought of as a continuously stratified, periodic version of the Phillips model. There is a further advantage to the present setup: In the Charney model, the zonal thermal wind of the base state is independent of the meridional coordinate and depth. Clearly the advantage of this assumption (and the constant scale-height assumption that lead to meridional gradient of potential vorticity being constant) is in reducing complexity and giving insights into the dynamics of baroclinic instability. However, in more realistic settings, baroclinicity is not uniform; it is more typical for it to be concentrated in zonal bands, as for example in the Antarctic Circumpolar Current or the jet-streams. The present setup, by generalizing the meridional and depth dependence of the zonal thermal wind to be periodic can represent the more typical non-uniform distribution of baroclinicity.

More fundamentally, of course, the question remains as to whether surface- and boundary-related processes are the only pathways that lead to a forward cascade of balanced energy. Indeed, e.g., as pointed out in Molemaker et al., 2005, the bulk of the balanced energy resides in the vertical interior and there is the alternative (spatially) more local route to dissipation directly through the interior turbulent cascade. This will be the second aim of the article—to explore the interior route to dissipation of balanced energy. We will do this by studying an initial value problem in which practically all of the energy in the initial condition resides at a scale close to the system size. But this initial condition is chosen to be baroclinically unstable, so that the occurrence of baroclinic instability initiates transfer of energy to smaller scales, primarily of course to the mesoscales. The resulting mesoscale shear and strain can then drive frontogenesis and the resulting frontal regions are susceptible to other unbalanced instabilities. This chain of events thus has the potential for establishing an interior pathway to dissipate balanced mesoscale energy. An aim of this article is to study this pathway, quantify the resulting small-scale dissipation, and establish its dependence on the Rossby number of the base flow.

2. The Small Rossby number and Froude number Regime

In this article, our interest is in a regime that is of relevance to ocean circulation (and to a certain extent to atmospheric circulation). In particular a) the horizontal scale of the domain (L) we are interested in corresponds to that of the oceanic mesoscales in the mid-latitudes (≈ 100 km corresponding to a few times the first internal Rossby deformation radius). The average depth of the ocean (H) is about 5km leading to a (vertical to horizontal) domain aspect ratio H/L of about 0.05, with this number being smaller yet if only the upper ocean were to be considered. At these scales, we are interested in b) the velocity-based Rossby number defined as $Ro = U/fL$ where U is peak velocity is small (say, < 0.1), and c) the velocity based (vertical) Froude number defined as $Fr = U/N_0H$ is small (say, < 0.1). For a comprehensive overview of the analytical treatment of the Boussinesq equations in this regime, see Babin *et al.* (1997). We note that since the nondimensional form of the rotating-stratified Boussinesq equations (see next section) have three non-dimensional parameters (e.g., Rossby number Ro , Froude number Fr , and vertical to horizontal aspect ratio \mathcal{R}), it is important that they all be considered when making comparisons of dynamic similarity to other studies. For example, we note that there are a number of studies that consider small Ro and Fr in a unit aspect ratio domain (e.g., see Bartello 1995; Smith & Waleffe 2002). Without getting into details, we suspect that vertical velocities in these flows tend to be higher than what is typical of oceanic mesoscales and submesoscales.

The smallness of the Rossby and Froude numbers of the initial condition we choose would be considered such as to lead to a balanced nonlinear flow evolution. One argument in favor of this point of view is as follows: The tendency of balanced quasi-two-dimensional turbulence to confine energy to the large and intermediate scales is accompanied by a forward cascade of potential enstrophy at small scales. The theoretical spectral scaling of the energy spectrum in this second inertial range corresponds to a steep -3 slope (Charney 1971). Such -3 (and steeper slopes due to the presence of coherent structures and other modeling artifacts) have repeatedly been verified numerically in both the quasi-geostrophic approximation (e.g., see Lesieur 1997) and the more complete non-hydrostatic Boussinesq description (e.g., see Bartello 1995). A consequence of such a steep spectral fall-off of the energy spectrum is that it precludes the possibility of increasing (appropriately defined scale dependent) Rossby number as the scale decreases. Thus, if Rossby number could not increase with decreasing scale, there would not be a route for

initially balanced, small Rossby and Froude number flows to break out of the scaling and become imbalanced. In the absence of external forcing and surface-related processes, it may therefore be tempting to think of this argument as a self-consistent explanation for why such flows should remain balanced.

However, there is the possibility that these arguments can fail in the context of the non-hydrostatic Boussinesq equations. A couple of heuristic lines of reasoning for why the above arguments can fail are as follows: It is possible that the nonlinear term in the definition of potential vorticity (see equations 3.3 and 3.4) could become increasingly important as resolution is increased. In such a situation, potential enstrophy would no more be a quadratic quantity, leaving total energy as the single (inviscidly) conserved quadratic (see section 3.3) invariant and opening up the possibility of a forward cascade of energy, a situation somewhat similar to three-dimensional turbulence.

From a more dynamical point of view, Hoskins et al., 1978 point out that in quasi-geostrophic theory, the role of *ageostrophic* motion is to restore thermal wind (geostrophic and hydrostatic) balance which the geostrophic motion is tending to destroy by changing the two parts of the thermal wind balance equally but in opposite directions. In this sense, the exact cancellation of the two tendencies by the ageostrophic velocity is more an artifact of the construction of the quasi-geostrophic approximation than it is a reflection of reality. Consequently, the ageostrophic velocity in the Boussinesq system could be such that it does not enforce exact cancellation and thus lead eventually to imbalanced motions.

Quasigeostrophy-related -3 (and steeper) scaling of the energy spectrum in the (full) enstrophy cascade range has been obtained in simulations of the Boussinesq equations (e.g. Waite & Bartello 2006). While shallower spectral slopes have been observed at the small-scale end of the enstrophy cascade range in other numerical simulations (e.g. Bartello 1995; Waite & Bartello 2006), they have typically been attributed to the large-scale Rossby number being large. (Note that the scale at which the break in slope appears is likely dependent on the choice of initial condition in the initial value problem and on the choice of forcing in the forced setting.)

That a shallow small-scale tail is always possible irrespective of how small the large-scale Rossby number is, is a possibility that has not been sufficiently considered. Indeed, we find that the scale at which the shallower slopes are seen decreases continuously when the large-scale Rossby number is reduced (see Fig. 19). This finding supports the above-mentioned possibility of a shallow tail at any large-scale Rossby number and at the same time highlights the high resolutions that are required to capture imbalanced motions when those Rossby numbers are small.

At this point, we digress to point out another difference in our experimental design. Previous studies of the initial value problem in the strongly rotating and strongly stratified flow regime that use the full nonhydrostatic Boussinesq equations have focussed mainly on statistics of the initial condition such as scale distribution of energy (e.g., Bartello 1995; Smith & Waleffe 2002; Waite & Bartello 2006, and others) . While we consider such statistics as well, our initial conditions are chosen to represent the unidirectional thermal-wind balance that is common place in both the atmosphere and the world oceans. Further, the baroclinic instability of such a flow is fundamental to atmospheric and oceanic circulation and it is the imbalance triggered by this instability that we consider.

The above discussion related to the nonlinear evolution of initially balanced flows implicitly assumed that imbalance is easily identified. However, this may not always be the case even though imbalance is associated with zero potential-vorticity modes. A simple way of recognizing the difficulty in identifying imbalance is to note the fact that

balance can exist at different orders. For example, optimal potential vorticity balance of Viúdez & Dritschel 2004 or that of McWilliams 1985 are balances at an order higher than that associated with thermal-wind. Thus the definition of balance can be complicated, there exists a substantial body of literature dedicated to it (e.g. see Viúdez & Dritschel 2004, and references therein), and it is an ongoing area of research. For this reason, we will take a pragmatic approach to imbalance in this article (while hoping to follow up on this issue in the future): Rather than diagnose imbalance from a dynamics perspective, we will use an energy perspective. This is because, from the point of view of energy in rotating stratified flows, it seems sufficient to consider those aspects of dynamics of a flow as balanced that tend to confine energy to large and intermediate scales. Other aspects of dynamics that lead to a forward cascade of energy can then be considered unbalanced.

As such, we will monitor various aspects of the flow to examine the possibility of forward cascade of energy over the course of nonlinear evolution of the baroclinically-unstable initial condition. At the lowest order, we will monitor domain-integrated dissipation of energy. Once robust behavior is seen in dissipation, we will examine spectral slopes. In the analysis of spectral slopes, the appearance of slopes shallower than -3 at the smaller of the resolved scales will be taken as an indicator of forward cascade resulting from unbalanced processes. In this sense, this study shares similarities with various previous studies in the atmospheric circulation modeling literature that attempt to explain the spectral slopes observed in Nastrom and Gage, 1985. Finally, and to a lesser extent we will examine the spectral flux of energy across scales using the framework of (3.8) to further validate our findings.

The rest of the paper is organized as follows. The next section describes the formulation of the problem. This is followed by a section on numerical simulations where nonlinear evolution of a particular flow configuration is analyzed in detail under the quasi-geostrophic approximation and under the non-hydrostatic Boussinesq approximation and at different resolutions. Evidence of imbalance is presented in this section. This is followed by a section where the scaling of dissipation with Rossby number is considered. After considering spectral scaling and spectral fluxes in the following section, we summarize and conclude with some discussion.

3. Problem Formulation

We consider the nonlinear evolution of a zonal flow that is in geostrophic and hydrostatic (thermal wind) balance in a stably-stratified environment

$$\rho(x, y, z, t) = \rho_0 + \rho_{env}(z) + \rho'(x, y, z, t)$$

and in a uniformly rotating Cartesian frame. In order to focus on the role of interior processes, boundaries are explicitly eliminated by considering the above evolution in a triply-periodic domain. The latter feature of the model setup is in common with numerous previous studies such as those of Bartello, 1995; Smith & Waleffe, 2002; Bartello, 2010 and others. We consider evolution under both the non-hydrostatic Boussinesq system that allows for imbalanced processes and the quasi-geostrophic system that allows for only balanced dynamics.

3.1. The Non-hydrostatic Boussinesq System

We write the non-hydrostatic Boussinesq equations in the nondimensional form as:

$$\frac{\partial \mathbf{u}_h}{\partial t} + \mathbf{u} \cdot \nabla \mathbf{u}_h + \frac{\mathbf{k} \times \mathbf{u}_h}{Ro} = -\frac{\nabla_h \phi}{Ro} + D_{\mathbf{u}_h}$$

B.T. Nadiga

$$\begin{aligned} \mathcal{R}^2 \left(\frac{\partial w}{\partial t} + \mathbf{u} \cdot \nabla w \right) &= -\frac{1}{Ro} \frac{\partial \phi}{\partial z} + \frac{b}{Fr} + D_w \\ \frac{\partial b}{\partial t} + \mathbf{u} \cdot \nabla b + \frac{w}{Fr} &= +D_b \\ \nabla \cdot \mathbf{u} &= 0. \end{aligned} \tag{3.1}$$

Here, beyond the usual notation, subscript h corresponds to horizontal (\mathbf{u}_h is the velocity vector in the horizontal—(x,y)—plane, and ∇_h is the horizontal gradient operator), w is the vertical velocity, b is buoyancy ($b = -\frac{g}{\rho_0} \rho'$) and where we have used D to represent the dissipation operator for brevity. The dissipation operator itself is discussed further later in this section.

The scales chosen for the non-dimensionalization above are such as to highlight the geostrophic and hydrostatic balance that is typical of large scale flow in the ocean and atmosphere and the small aspect ratio of the domains in which such flow occurs. In particular, horizontal lengths are non-dimensionalized by L , the horizontal length of the domain (square in the x-y directions), vertical lengths by H , the depth of the domain (z direction), horizontal velocities by U the peak velocity of the initial zonal flow, time by L/U , vertical velocities by UH/L (cf. divergence free condition), dynamic pressure by $\rho_0 fUL$ (cf. geostrophy) where f is the Coriolis frequency on the f-plane we consider, and perturbation buoyancy by UN_0 (in quasi-geostrophy, $b = f\partial\psi/\partial z$; $N_0H \approx fL$) where N_0 is the Brunt-Vaisala frequency given by

$$N_0 = \sqrt{-\frac{g}{\rho_0} \frac{d\rho_{env}}{dz}}. \tag{3.2}$$

Finally we note that U is the scale of the geostrophic velocity in balance with buoyancy b .

3.2. The Quasi-Geostrophic Approximation

The above Boussinesq system conserves a potential vorticity (e.g., see Bartello 1995) given by

$$Q = \boldsymbol{\omega}_a \cdot \nabla b = (\boldsymbol{\omega} + f\hat{\mathbf{z}}) \cdot (N_0^2 \hat{\mathbf{z}} + \nabla b) = fN_0^2 + \left(\zeta N_0^2 + f \frac{\partial b}{\partial z} \right) + \boldsymbol{\omega} \cdot \nabla b, \tag{3.3}$$

where $\boldsymbol{\omega}$ is (relative) vorticity $\boldsymbol{\omega}_a$ is absolute vorticity, ζ is the vertical component of relative vorticity and the first, second and third terms are respectively independent, linear and quadratic in velocity and buoyancy variables. The nondimensional form is given by

$$Q = 1 + Ro\zeta + Fr \frac{\partial b}{\partial z} + RoFr \boldsymbol{\omega} \cdot \nabla b, \tag{3.4}$$

where all variables are now nondimensional. However, (3.3) or (3.4) cannot be inverted to obtain *all* dynamical quantities of interest since there are other modes—those with zero potential vorticity—that evolve as well. Therefore, inverting potential vorticity or an approximation of it (e.g., its linearization) is useful only to the extent that it can help diagnose the balanced component.

In the low Rossby number, low Froude number regime that we are concerned with in this article, the large-scale, low-frequency modes of the system are well described by the quasi-geostrophic approximation. This system is obtained by making the hydrostatic approximation ($\mathcal{R} \ll 1$) and performing asymptotic analysis of the above equations using Ro and Fr as small parameters (e.g., see Vallis 2006); the quasi-geostrophic approximation

is obtained at the lowest order in Ro and Fr . In this approximation, advection is reduced to that by the horizontally non-divergent horizontal geostrophic velocity and buoyancy is related to the vertical derivative of the geostrophic streamfunction as

$$b = \frac{Fr}{Ro} \frac{\partial \psi}{\partial z}$$

(dimensionally $b = f \frac{\partial \psi}{\partial z}$). In the inviscid adiabatic limit, the buoyancy equation reduces to

$$\frac{\partial b}{\partial t} + \mathbf{u}_g \cdot \nabla_h b = -\frac{w}{Fr}, \quad (3.5)$$

and the curl of the horizontal momentum equation reduces to

$$\frac{\partial \zeta}{\partial t} + \mathbf{u}_g \cdot \nabla_h \zeta = -\frac{1}{Ro} \frac{\partial w}{\partial z}. \quad (3.6)$$

On eliminating w from (3.6) and (3.5), evolution of the system can be described in terms of a single scalar, the quasi-geostrophic potential vorticity:

$$\begin{aligned} \frac{\partial q}{\partial t} + \mathbf{u}_h \cdot \nabla_h q &= 0 \\ q &= \nabla_h^2 \psi + \frac{Fr^2}{Ro^2} \frac{\partial^2 \psi}{\partial z^2} \end{aligned} \quad (3.7)$$

where an f-plane and constant stratification have been assumed. In this case, the quasi-geostrophic potential vorticity can be inverted to obtain all relevant quantities in the approximation. In particular once the scaled-Laplacian is inverted to obtain ψ , the streamfunction, $\mathbf{u}_h = \hat{\mathbf{z}} \times \nabla_h \psi$. Finally, comparing the expressions for potential vorticity in (3.7) and (3.4), the quasi-geostrophic potential vorticity is seen to be the linear component of potential vorticity that is conserved in the Boussinesq system. (The absence of the constant term in (3.7) leads it to be qualified further as perturbation quasi-geostrophic potential vorticity.)

3.3. Energy Equation

Kinetic energy (per unit mass) is defined in the usual fashion as

$$k = \frac{1}{2} (\mathbf{u}_h^2 + \mathcal{R}^2 w^2),$$

and the available potential energy (per unit mass) as

$$p = \frac{b^2}{2},$$

where the quantities are averaged over the volume of interest and noting that the variables are non-dimensional. (In the dimensional form $p_d = b_d^2 / (2N_0^2)$ where the subscript d stands for “dimensional”.)

The equations for the evolution of kinetic energy and potential energy are easily formed starting from (3.1) by taking the dot product of the momentum equation with velocity and multiplying the buoyancy equation by the perturbation buoyancy. They may be found in textbooks (e.g., see Vallis 2006) and since we do not require the details of those equations, we will not reproduce them here. However, we note that integrating the kinetic and potential energy equations over the domain and summing the two equations leads to

$$\frac{dT}{dt} = -D,$$

where $T = K + P$ is the domain-integrated total energy, K and P domain-integrated kinetic and potential energy respectively and D is the domain-integrated dissipation of total energy by small scale dissipation.

In order to better understand dynamics including that of dissipation, besides studying the evolution of domain-integrated energy, we will also consider the flux of energy across scales. For this purpose, we take the dot product of the Fourier transform of the momentum (buoyancy) equation in (3.1) and the conjugate of the Fourier transform of velocity (buoyancy) to arrive at equations that describe the evolution of energy in a scale-wise fashion:

$$\begin{aligned}\frac{d\mathcal{K}(\boldsymbol{\kappa})}{dt} + \mathcal{K}_{tr}(\boldsymbol{\kappa}) &= \mathcal{PW}_{tr} + \mathcal{BF}_{tr} + \mathcal{D}_{\mathcal{K}}(\boldsymbol{\kappa}) \\ \frac{d\mathcal{P}(\boldsymbol{\kappa})}{dt} + \mathcal{P}_{tr}(\boldsymbol{\kappa}) &= -\mathcal{BF}_{tr} + \mathcal{D}_{\mathcal{P}}(\boldsymbol{\kappa}) \\ \frac{d\mathcal{T}(\boldsymbol{\kappa})}{dt} + \mathcal{T}_{tr}(\boldsymbol{\kappa}) &= \mathcal{PW}_{tr} + \mathcal{D}_{\mathcal{T}}(\boldsymbol{\kappa}),\end{aligned}\tag{3.8}$$

where $\mathcal{T}_{tr}(\boldsymbol{\kappa}) = \mathcal{K}_{tr}(\boldsymbol{\kappa}) + \mathcal{P}_{tr}(\boldsymbol{\kappa})$ is the nonlinear scale transfer of total energy, with $\mathcal{K}_{tr}(\boldsymbol{\kappa})$, $\mathcal{P}_{tr}(\boldsymbol{\kappa})$ representing the nonlinear scale transfer of kinetic and potential energy respectively, and $\mathcal{D}_{\mathcal{T}}(\boldsymbol{\kappa}) = \mathcal{D}_{\mathcal{K}}(\boldsymbol{\kappa}) + \mathcal{D}_{\mathcal{P}}(\boldsymbol{\kappa})$ is scale-wise dissipation. In other notation, \mathcal{PW}_{tr} stands for the scale transfer of kinetic energy by pressure work and \mathcal{BF}_{tr} represents the scale transfer of kinetic/potential energy by buoyancy flux.

For convenience, we consider only the shell-averaged version of this equation (one-dimensional form) and prefer the nonlinear flux of energy across scales \mathcal{T}_f , \mathcal{K}_f , and \mathcal{P}_f —obtained as integrals of the respective transfer as

$$\mathcal{T}_f(k) = \int_0^k \mathcal{T}_{tr} dk.$$

3.4. Initial Conditions

We choose the initial condition to be in geostrophic thermal-wind balance:

$$\frac{\partial}{\partial z}(v, -u) = \frac{Ro}{Fr} \nabla_h b, \quad w = 0\tag{3.9}$$

where, as before (u, v, b) represents a perturbation about the stably stratified no-flow hydrostatic equilibrium. A particular form of the perturbation b that further satisfies periodicity is of the form:

$$b(x, y, z) = \cos(2\pi k_x x) \cos(2\pi k_y y) \cos(2\pi k_z z),\tag{3.10}$$

somewhat reminiscent of the Taylor-Green vortex solution, but now in the extended velocity and buoyancy variables, and with velocity given by (3.9) (also see Simon & Nadiga 2014). In (3.10), k_x , k_y , and k_z are the non-dimensional wavenumbers in the three spatial directions. After noting that uni-directional flows in this set are exact solutions of the inviscid adiabatic equations, we choose the gravest uni-directional (horizontal) flow with no variations in the flow direction as the base state. In particular, we choose the flow to be zonal and with no variations in the zonal (x) direction ($k_x = 0, k_y = 1, k_z = 1$):

$$b(x, y, z; t = 0) = \cos(2\pi k_y y) \cos(2\pi k_z z),\tag{3.11}$$

The initial buoyancy $(-g(\rho_{env} + \rho')/\rho_0)$ is plotted in the nondimensional form as $z + Fr b$, zonal velocity, and potential vorticity fields are shown in Fig. 1. These fields are for the specific Rossby and Froude numbers to be considered in the next section. For the other Rossby and Froude numbers considered in this article, it should be clear that

the buoyancy and zonal velocity fields are simply scaled by the respective Froude and Rossby numbers. Further, for the other Rossby and Froude numbers, the structure of the potential vorticity field remains visually indistinguishable. This is because, and as discussed further, over the range of Rossby and Froude numbers considered, the quadratic term in the definition of potential vorticity is small.

It is easy to see that the quasi-geostrophic potential vorticity of the unidirectional base flow is proportional to $\cos(2\pi y)\sin(2\pi z)$. This can also be seen in the right panel of Fig. 1. This form satisfies the Charney-Stern-Pedlosky necessary condition for baroclinic instability which requires that $\partial q/\partial y$ change sign in the domain (e.g., see Vallis 2006).

For the Boussinesq system, the linear term in (3.4) is likewise proportional to $\cos(2\pi y)\sin(2\pi z)$ as seen in the expression for potential vorticity of the base state in (3.12):

$$Q(x, y, z; t = 0) = 1 + Ro \left(1 + \left(\frac{Fr}{Ro} \right)^2 \right) \frac{\partial b}{\partial z} + Ro^2 \left(\frac{Fr}{Ro} \right)^2 \left[\left(\frac{\partial b}{\partial z} \right)^2 - \left(\frac{\partial b}{\partial y} \right)^2 \right]. \quad (3.12)$$

For the Boussinesq system, initial conditions considered in this article are such that Fr/Ro , the ratio of the domain size to Rossby radius, is held fixed. Consequently, for these cases, the ratio of the magnitude of the quadratic term to the magnitude of the linear term ($1.6\pi Ro$) is between 0.10 and 0.17.

Although the initial conditions satisfy the necessary condition for instability, integration of the unidirectional flow over several tens of eddy turnover times did not lead to a destabilization of the base flow solution. That is to say, the truncation errors were too small to destabilize the flow in a reasonable length of time. Therefore, a further set of uni-directional thermal-wind modes that are again individually exact solutions were superposed on the base flow. These modes were chosen to have an energy spectrum that fell off steeply as $(k_h k_z)^{-8}$ (essentially confined to the largest scales), and to contain a small fraction of the energy of the unidirectional base flow (approximately 0.05%); these perturbations cannot be seen in Fig. 1).

3.5. Numerical Discretization and Consistency Between Horizontal and Vertical Resolutions

A standard fully-dealiased Fourier pseudo-spectral method is used for the spatial discretization and the equations are integrated in time using a fourth order Runge-Kutta scheme. The above discretization, as implemented in parallel using MPI in the Sandia-LANL DNS code (Taylor *et al.* 2003) forms the computational kernel used for the simulations.

We next consider the issue of consistency between horizontal and vertical resolutions. In quasi-geostrophic dynamics horizontal scales ΔL and vertical scales Δz are related as (e.g., see Lindzen & Fox-Rabinovitz 1989)

$$\frac{\Delta L}{\Delta z} = \frac{N_0}{f},$$

where ΔL is related to the Rossby radius. It is clear that the quasi-geostrophic approximation is applicable to horizontal scales of the order of the first Rossby radius. However, we'll presently be considering quasi-geostrophic simulations simply as balanced counterparts (controls) of the unbalanced Boussinesq simulations, and for this reason, the quasi-geostrophic simulations will consider horizontal scales much smaller than the first Rossby radius. Thus if the smallest Rossby radius that is resolved is of the order of the grid resolution Δx , then to adequately resolve that mode in the vertical, the vertical

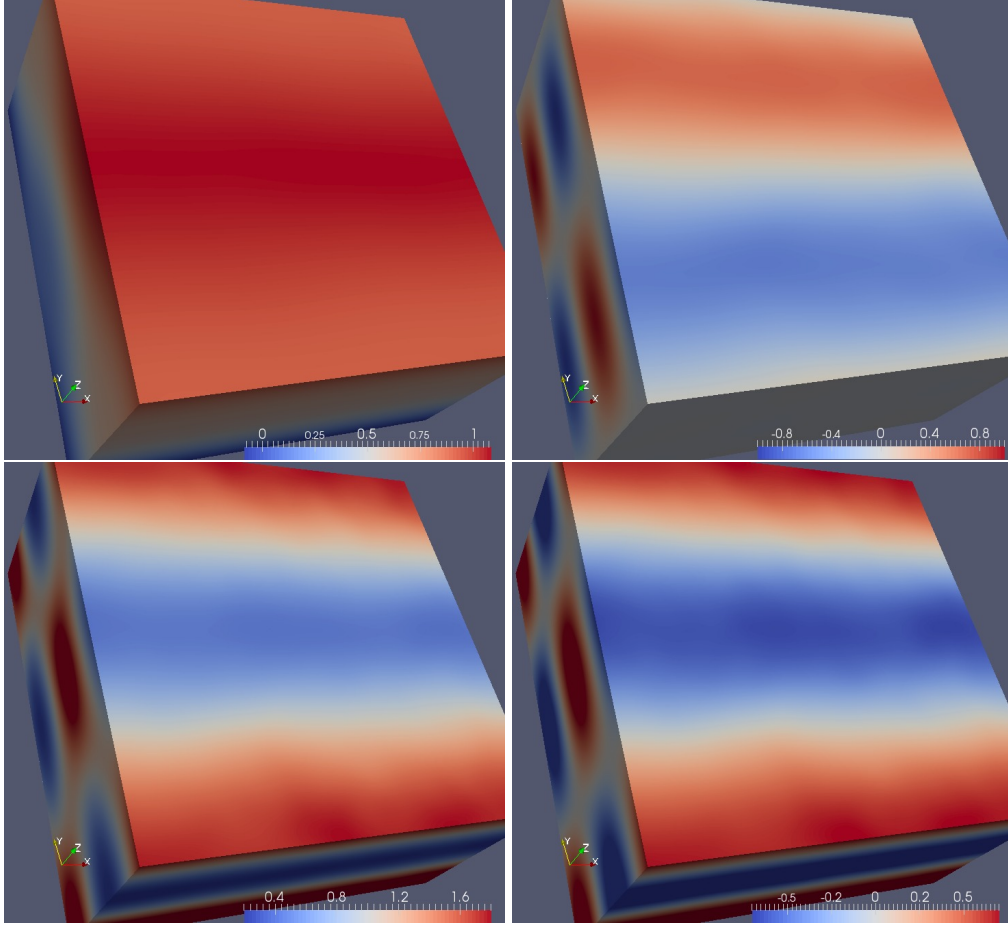


FIGURE 1. Initial conditions: Buoyancy (top left), zonal velocity (top right), and potential vorticity (bottom left) for the Boussinesq system. Perturbation potential vorticity for the QG system (bottom right). The vertical has been exaggerated by a factor of 10. The actual vertical extent is a twentieth of the horizontal extent.

resolution has to satisfy

$$\Delta z = \frac{f}{N_0} \Delta x. \quad (3.13)$$

On the other hand, in the nonhydrostatic Boussinesq system, when fronts occur, their (vertical to horizontal) aspect ratio scale as f/N_0 (e.g., see Snyder *et al.* 1993). When frontal collapse occurs, there is a cascade of energy to grid scales, impeded only by the small scale viscosity and diffusion (parameterized here by hyperviscosity and hyperdiffusivity). Therefore, if fronts are to be adequately resolved, vertical resolution will again have to satisfy requirement (3.13). As pointed out in these references, if the resolution requirement (3.13) is not met, spurious dynamics including spurious gravity wave activity can occur and incorrect numerical solutions are possible. All numerical simulations presented here satisfy the above resolution requirement.

3.6. Small scale dissipation

If an isotropic Laplacian dissipation operator were to be used, as in the Navier-Stokes equations, the prognostic governing equations would be

$$\begin{aligned}
 \frac{\partial \mathbf{u}_h}{\partial t} + \mathbf{u} \cdot \nabla \mathbf{u}_h + \frac{\mathbf{k} \times \mathbf{u}_h}{Ro} &= -\frac{\nabla_h \phi}{Ro} + \frac{1}{Re} \left(\nabla_h^2 \mathbf{u}_h + \frac{1}{\mathcal{R}^2} \frac{\partial^2 \mathbf{u}_h}{\partial z^2} \right) \\
 \mathcal{R}^2 \left(\frac{\partial w}{\partial t} + \mathbf{u} \cdot \nabla w \right) &= -\frac{1}{Ro} \frac{\partial \phi}{\partial z} + \frac{b}{Fr} + \frac{Pr}{Re} \left(\mathcal{R}^2 \nabla_h^2 w + \frac{\partial^2 w}{\partial z^2} \right) \\
 \frac{\partial b}{\partial t} + \mathbf{u} \cdot \nabla b + \frac{w}{Fr} &= +\frac{1}{Re} \left(\nabla_h^2 b + \frac{1}{\mathcal{R}^2} \frac{\partial^2 b}{\partial z^2} \right)
 \end{aligned} \tag{3.14}$$

where Re is the Reynolds number and Pr is the Prandtl ratio, the ratio of buoyancy diffusivity to viscosity. In each of the three equations above, the ratio of vertical dissipation to horizontal dissipation is $\frac{1}{\mathcal{R}^2}$. Thus, with the small aspect ratio domains that we are interested in (atmospheres and oceans), vertical dissipation is seen to dominate horizontal dissipation. Furthermore, the dynamical scales of interest in this study are in the range of hundreds of meters to tens of kilometers, many orders of magnitude larger than the Kolmogorov dissipation scales at which an isotropic Laplacian dissipation would be appropriate. For these reasons, the computations are more in the nature of Large Eddy Simulations rather than Direct Numerical Simulation of the Navier-Stokes equations. Furthermore, in atmosphere and ocean settings, at the scales of interest, diapycnal mixing coefficients are orders of magnitude smaller than isopycnal mixing coefficients. Therefore, as is common practice (e.g., Molemaker *et al.* 2010) we choose a simple hyperviscous but anisotropic dissipation operator that localizes dissipation to the smallest of the resolved scales and set the (eddy) Prandtl ratio to unity. The dissipation operator is therefore of the form

$$\nu \left(\nabla_h^2 + \frac{\nu_v}{\nu} \frac{\partial^2}{\partial z^2} \right)^n .$$

In order to confine the effects of dissipation to the smallest of the resolved scales and to extend the inertial range, an eighth order hyper-diffusion operator was used for the dissipation of both momentum and buoyancy. For the main sequence of simulations considered in the article ν in the above equation is determined so that the hyperviscous-Reynolds number based on the grid scale is no more than four. For the reference case with $Ro = 0.03$, the simulation was repeated with various variations to the small-scale dissipation operator to study dependence of results on them. For example, Fig. 23 shows dissipation spectra and spectral flux of kinetic energy in two such simulations with increased viscous and diffusive coefficients (grid Reynolds number less than 1.6 and 0.4). There is no discernible trend in the dissipation spectra for the three cases other than the location of the peak itself and the differences are small. Further, over the range of wavenumbers where there is a forward cascade of energy in the main panel of Fig. 23, while the least dissipative case (the reference case) shows a larger flux at both the lower and upper ends of this range, the trend is reversed over the intermediate range of scales. Further, in otherwise identical experiments, we have experimented with the scaling used in Chasnov (1994) to determine the value of ν , and found the two methods to lead to remarkably similar temporal profiles of dissipation rate. These results suggest the robustness of the results we present to the parameterization of small-scale dissipation.

Finally, we note that inevitable artifacts of finite resolution lead to a certain fraction of energy cascading forward (e.g. see footnote on page 264 in Nadiga & Straub 2010, for an estimate of this fraction). This is evident in simulations of (interior) quasi-geostrophic

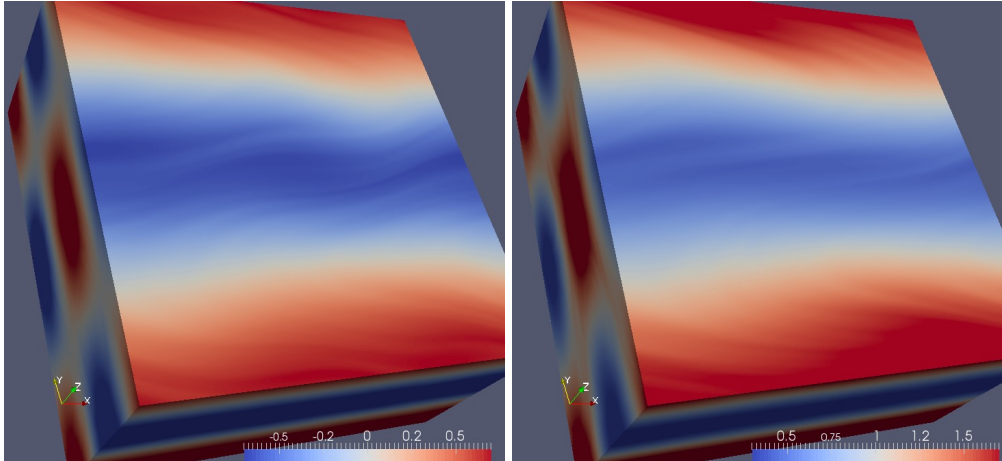


FIGURE 2. Growth of the unstable baroclinic wave at time 1.2 for the QG system in the left panel and for the Boussinesq system in the right panel. Potential vorticity is plotted.

turbulence (or two-dimensional turbulence), which dynamics is by definition balanced. We will account for this effect approximately by considering dissipation and dynamics of twin simulations using the quasi-geostrophic approximation and comparing results.

4. Nonlinear Flow Evolution

Our interest is in the parameter regime where the velocity-based Ro and the (vertical) velocity-based Fr , both based on the domain scales are small and the domain itself is such that the aspect-ratio \mathcal{R} is small. Further, we will hold the ratio Fr/Ro , which is the ratio of the horizontal size of the domain to the first internal Rossby deformation radius, fixed at two. (The most unstable wavelength in this setup is shorter than the corresponding wavelength in the Eady problem by a factor of about two.) Based on these considerations, we choose a reference set $\mathcal{R} = 0.05$, $Ro = 0.03$, and $Fr = 0.06$. We are in the process of conducting linear stability analysis of the particular flow configuration used in this study and will report on it in the near future.

Initial conditions for these values of the parameters are shown in Fig. 1. The color scale for potential vorticity in the QG and Boussinesq systems are chosen to be symmetric about the ambient value. Nevertheless, visual differences in the potential vorticity field between the two system are evident if the lower panels of Fig. 1. For this reason, we caution the reader that spatial plots of fields should be used only as an aide in visualizing flow and qualitative differences in evolution between the two systems.

We now consider the evolution of the above initial conditions under both quasi-geostrophic dynamics and the non-hydrostatic Boussinesq dynamics. Further, in order to establish the role of resolution, we consider evolution under the QG approximations at two different resolutions and that under the Boussinesq equations at three different resolutions. The two common resolutions correspond to spanning the (nondimensional) unit length in the horizontal by 480 (1x) and 960 (2x) points. The third resolution considered for the Boussinesq system is intermediate between the above two resolutions: 720 (1.5x). At each of these horizontal resolutions, the vertical resolution is chosen to satisfy requirement (3.13).

With the above choice of initial conditions that consisted of a unidirectional base flow and perturbations, each of which was individually balanced, the unidirectional base flow

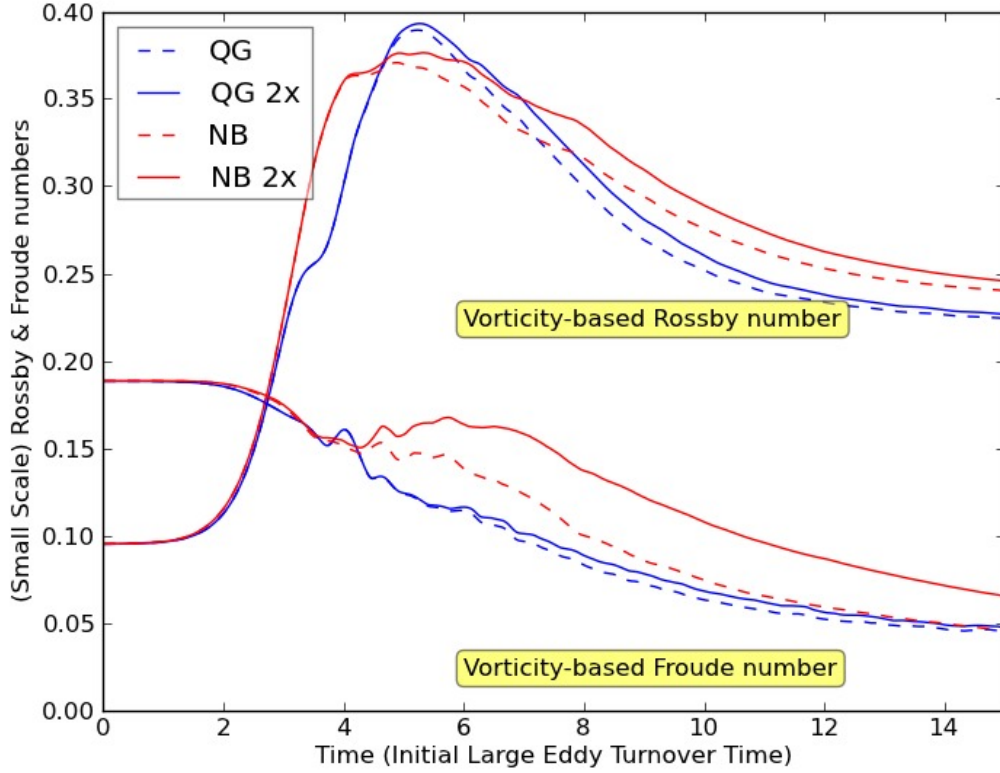


FIGURE 3. Evolution of the rms of the vorticity-based Rossby and Froude numbers $((\zeta/f)_{(rms)}; (\omega_h/N_0)_{(rms)})$ under the QG and Boussinesq approximations. Initial evolution is seen to be similar under the two approximations and at different resolutions. Evolution in the later part of the instability phase is seen to be different in the two systems with suggestions of an instability other than the initial geostrophic hydrostatic baroclinic instability in the Boussinesq system.

was readily destabilized and the process of geostrophic hydrostatic baroclinic instability unfolded. Figure 2 shows the growth of the unstable baroclinic wave at time 1.2 for the QG system in the left panel and for the Boussinesq system in the right panel; in these figures potential vorticity is plotted. We note here that time is non-dimensionalized by the initial eddy turnover time and that the characteristic eddy turnover at later times is less than the chosen initial eddy turnover time. Besides similarities in the gross flow structure, what is clear in this figure is that there are significant differences in the growing perturbations even at this early time. However, a characterization of these differences will have to await the completion of linear stability analysis presently underway.

4.1. Evolution of vorticity-based Rossby and Froude numbers and other relevant limits

The velocity-based Rossby and Froude numbers of the initial conditions serve, at best, as a rough guide and could in some cases be misleading (as, e.g., in a setup where the domain scale is much greater than the deformation radius). For this reason, we compute the vorticity-based Rossby and Froude numbers; not only do they serve as dynamically relevant counterparts of the velocity-based ones, but they also emphasize the smaller

scales. They are defined respectively as

$$Ro_\omega = \frac{\zeta}{f}, \quad (4.1)$$

where ζ is the vertical component of relative vorticity and

$$Fr_\omega = \frac{|\omega_h|}{N_0}, \quad (4.2)$$

where $|\omega_h|$ is the magnitude of the horizontal components of relative vorticity. Figure 3 shows the evolution of rms values of vorticity-based Rossby and Froude numbers. $Ro_\omega^{(rms)}$ is seen to remain at its initial value over the first couple initial-eddy-turnover times, after which, it begins to increase as the unstable baroclinic wave begins to wind up. In both systems, $Ro_\omega^{(rms)}$ reaches its peak value of about 0.4 at about time 5 after which it begins to fall. While there is overall similarity in the evolution of $Ro_\omega^{(rms)}$ in the two systems, it is to be noted that a) the peak value of $Ro_\omega^{(rms)}$ is higher in the QG system than in the Boussinesq simulations whereas at late times $Ro_\omega^{(rms)}$ is lower in the QG system, and b) the ascent and descent around the peak is temporally more extended in the Boussinesq system. As to whether the latter behavior is due to the possibility of other instabilities than the hydrostatic geostrophic baroclinic instability in the Boussinesq system unlike in the QG system is not clear.

$Fr_\omega^{(rms)}$ is seen to display a decreasing trend through the instability phase although the behavior is not monotonic. This behavior is consistent with the conversion of the vertical shear of horizontal velocity (main component of horizontal vorticity) into horizontal shear of horizontal velocity associated with baroclinic instability. Further, $Fr_\omega^{(rms)}$ is seen to be higher in the Boussinesq system most of the time. Two possible scenarios that could result in such larger values are a) If the horizontal vorticity is balanced, then it could be that the conversion of initial potential energy into kinetic energy is smaller in the Boussinesq system, or b) there is a significant amount of unbalanced horizontal vorticity.

Finally, we note that while there is overall agreement in the behavior of $Ro_\omega^{(rms)}$ and $Fr_\omega^{(rms)}$ between the simulations at the two resolutions, there is a greater dependence on resolution in the Boussinesq system.

McWilliams *et al.* 1998 consider the solvability limits of a version of balance equations formulated in isentropic coordinates (see references therein) and conjecture that those limits coincide generally with the boundary between distinctive nonlinear dynamical behaviors associated with large-scale and small-scale regimes. The reader is referred to the above article for details; the limits are also reviewed in Molemaker *et al.*, 2005. In brief, the above limits are related to changes in sign of a) stratification (gravitational instability), b) absolute vorticity A (centrifugal or inertial instability):

$$A < 0, \quad A = f + \zeta, \quad (4.3)$$

and c) the difference between absolute vorticity and the horizontal strain rate S (anticyclonic ageostrophic baroclinic instability):

$$A - S < 0, \quad S = \sqrt{(u_x - v_y)^2 + (v_x + u_y)^2}. \quad (4.4)$$

They further suggest that these limits are likely, approximately, indicative of the transition from the larger-scale regime of inverse energy cascades by anisotropic flows to the smaller-scale regime of forward energy cascade to dissipation by more isotropic flows and intermittently breaking inertia-gravity waves. We also note here that there is some work to suggest that the last two of the above kinds of instability may be dynamically

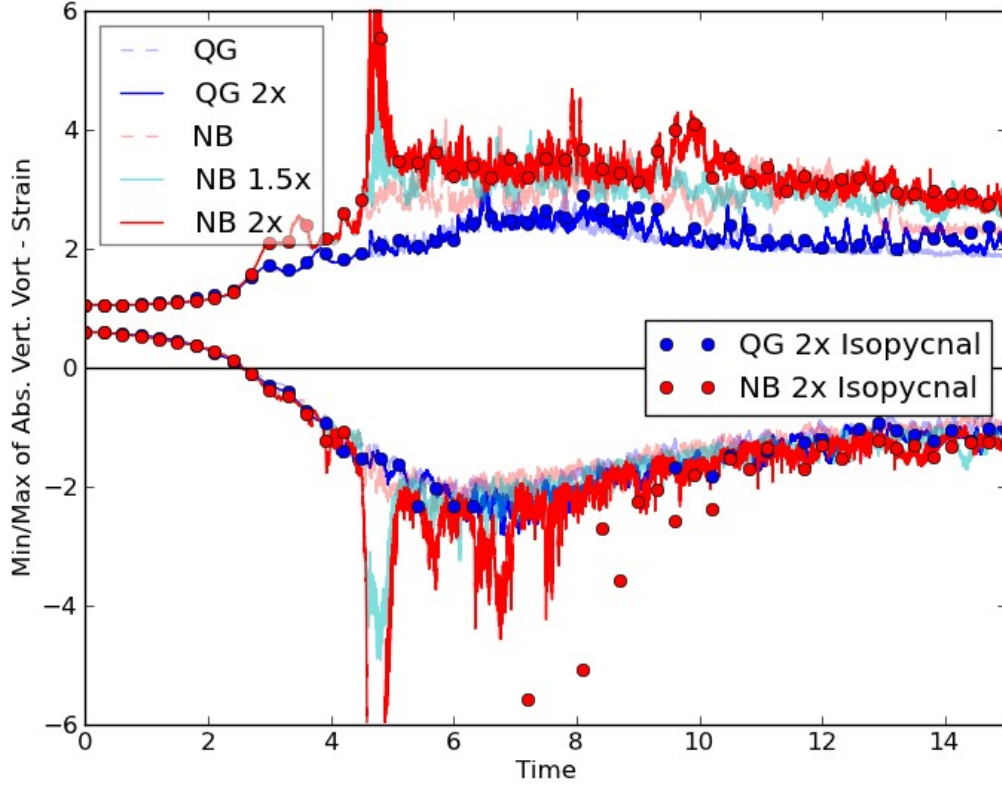


FIGURE 5. Evolution of peak values of the difference between absolute vorticity and strain. Change in sign of this quantity in the QG approximation, if only locally, suggests in-applicability of that approximation in those regions. There is general agreement in the evolution of this quantity in the QG and Boussinesq approximations.

every 0.3 time units. Up to times when peak values of R_{ω} first cross unit magnitude, the values of R_{ω} computed on the horizontal and isopycnal match well. This is largely the case at late times ($t > 12$) as well; large differences are confined to intermediate times.

In Fig. 3, the domain averaged (rms) values of R_{ω} are seen to remain less than 0.4. However, Fig. 4 shows an extended period of time when the peak values of R_{ω} are greater than unity in the QG approximation (likewise with the Boussinesq system). This is suggestive of spatially and temporally intermittent events that lead to $O(1)$ R_{ω} locally. The occurrence of $O(1)$ R_{ω} in the quasi-geostrophic system in localized regions is indicative of the in-applicability of the approximation in those regions and in particular, the second condition for the loss of integrability, equivalent to the minimum of R_{ω} falling below unity, is seen to be met in the QG simulations, first at a time close to 3.3.

Further, we note that a) In contrast to the behavior of the rms, peak values of R_{ω} are higher in the Boussinesq system suggesting greater intermittency in the Boussinesq system compared to the QG system. b) Increased resolution leads to higher levels of intermittency in the Boussinesq system. c) A greater degree of asymmetry is seen between cyclones and anticyclones in the Boussinesq system—peak cyclonic values are stronger than peak anticyclonic values. d) The QG approximation reproduces the minimum value of R_{ω} (peak anti-cyclonic values) found in the Boussinesq system remarkably well other than in (likely) frontal regions. It fares much worse in the cyclonic region.

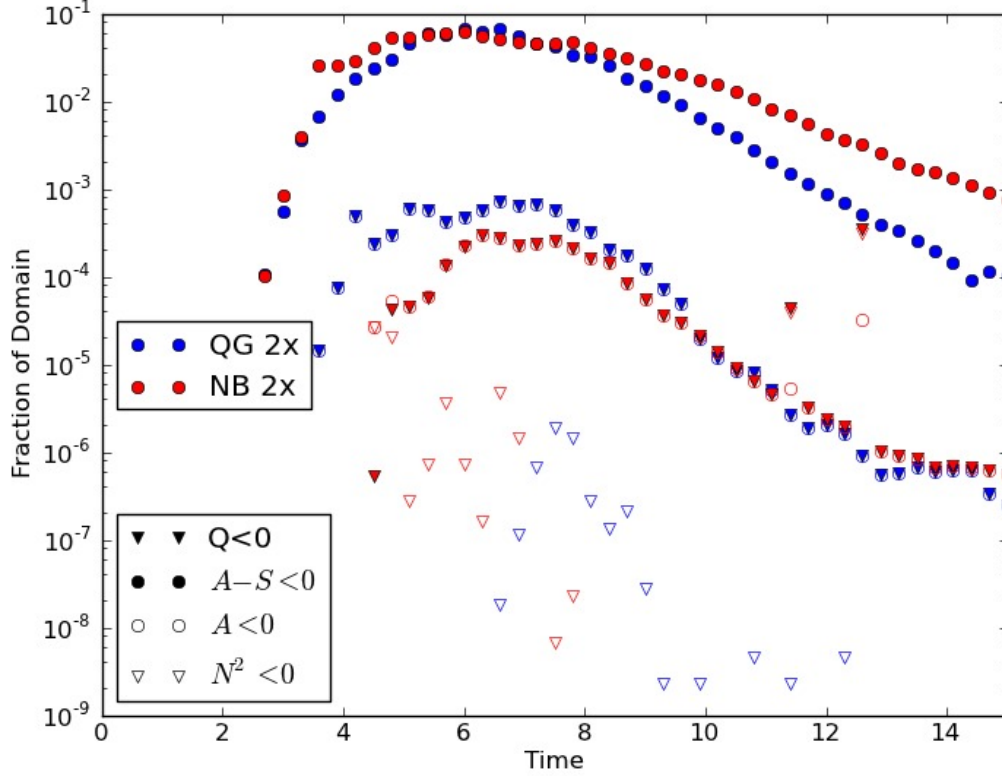


FIGURE 6. Evolution of the fraction of domain where certain dynamical limits are crossed in the QG and Boussinesq systems. The limits are indicated in the lower legend and correspond to (a) negative potential vorticity, (b) $A - S < 0$ where A is absolute vertical vorticity and S is the magnitude of strain as defined in (4.4), (c) $A < 0$, and (d) $N^2 < 0$.

In order to better diagnose dynamics and for future reference, Fig. 4 shows in the inset plot the time evolution of the peak value of the vorticity based Froude number Fr_ω . In this figure, the time of occurrence of maxima may be seen to be approximately the same as the time of occurrence of extrema in Ro_ω . While the peak value in the QG system is close to one, much higher values are attained in the Boussinesq system. Comments about increased intermittency in the Boussinesq system made in the context of Ro_ω hold for the Fr_ω diagnostic as well.

We also monitor $A - S$ as relates to the third of the balanced-integrability conditions above. Figure 5 shows the evolution of the peak values of $A - S$. Again, while lines show values obtained with horizontal derivatives evaluated at constant z , circles show values obtained using horizontal derivatives on isopycnal surfaces. For this diagnostic, differences between the two values are large only in anticyclonic regions at intermediate times.

The change in sign of $A - S$ as the baroclinic instability unfolds in the QG system further confirms the violation of the integrability condition for the QG system in localized regions seen in the previous diagnostics. Indeed, the requirement that the change in sign of this diagnostic should occur earlier than the violation of the second solvability condition is confirmed: $A - S$ changes sign at a time close to 2.5 where as A changes sign at around 3.3. Further, it is possible that the increase in the maximum of Ro_ω in the Boussinesq

system at time 2.5 is related to the change in sign of $A - S$. These diagnostics are then consistent with the possibility that the dynamical conditions are conducive for the occurrence of the anticyclonic ageostrophic baroclinic instability of McWilliams *et al.* 1998 (as distinct from gravitational and centrifugal instabilities) in the context of a set of governing equations that do not make the geostrophic balance approximation.

Next, Fig. 6 shows fractions of the domain where the three solvability limits are violated for the QG system as a function of time. Also shown is the fraction of domain where quasi-geostrophic potential vorticity falls below -1 (indicated as $Q < 0$ where $Q_{qg} = 1 + q$ and q is given by (3.7)). Here it is seen that the violation of the $A - S$ criterion is most extensive and reaching a value of about 8% of the domain at around time 6.5. As mentioned earlier, that this condition is violated most extensively is expected and related to the fact that this condition occurs at a smaller value of the local Rossby number as compared to, say, the absolute vorticity criterion. The latter $A < 0$ is next most often violated with violations of static stability being very infrequent. Further, a very high degree of correlation is seen between the fraction of the domain where potential vorticity is negative and where absolute vertical vorticity is negative suggesting that the flow may be susceptible to centrifugal and inertial instabilities.

Given the conjecture of McWilliams *et al.* 1998 of the relevance of these limits to the transition from the larger-scale regime of inverse energy cascade to the smaller-scale regime of forward energy cascade, fractions of the domain where these conditions are met in the Boussinesq system are shown in Fig. 6 as well. This will be useful later in interpreting dynamics in the Boussinesq system. We note, however, that there is generally a good correspondence in this diagnostic between the two systems. In particular, the strong correlation seen between the fraction of the domain where potential vorticity is negative and where absolute vertical vorticity is negative in the QG system holds in the Boussinesq system as well.

4.2. Evolution in the QG System

Given the small Rossby and Froude numbers of the initial condition in the thin aspect ratio domain we consider, the general aspects of the flow evolution under the QG and Boussinesq systems are similar and consistent with those expected from geostrophic turbulence theory. Initial evolution of the smooth initial condition consists of a linear phase when the most unstable baroclinic perturbation grows. Subsequent (nonlinear) evolution of the instability leads to a roll-up into eddies. The break-up of the flow and subsequent nonlinear evolution leads to an inverse cascade of energy that results in a build up of energy in the barotropic mode. Energetically the large-scale aspect of flow evolution comprises a conversion of available potential energy of the initial condition to eddy kinetic energy followed by an inverse cascade of kinetic energy.

In order to convey a qualitative picture of the flow evolution, Figure 7 shows the distribution of potential vorticity in the QG system at a few selected times. Looking back at Figs. 4 and 5, we choose the following four times: a) time 4.8 which is close to the time of a local peak of maximum Ro_ω , b) time 6.1 which is close to the time of global minimum of $A - S$, c) time 6.4 which is close to the time of both the global minimum of Ro_ω and global maximum of Fr_ω , and d) time 7.0 which is close to the global maximum of Ro_ω . We note that the global maximum of the rms of Ro_ω occurs at time 5.2 which is close to the time of the top-left snapshot.

Over the range of times considered, a progressive destabilization of smaller scales of the flow with time is evident from these snapshots and they may be thought of as instabilities associated with various baroclinic modes of the system. We note here that given the spatially-variable nature of the vertical shear of zonal velocity and stratification

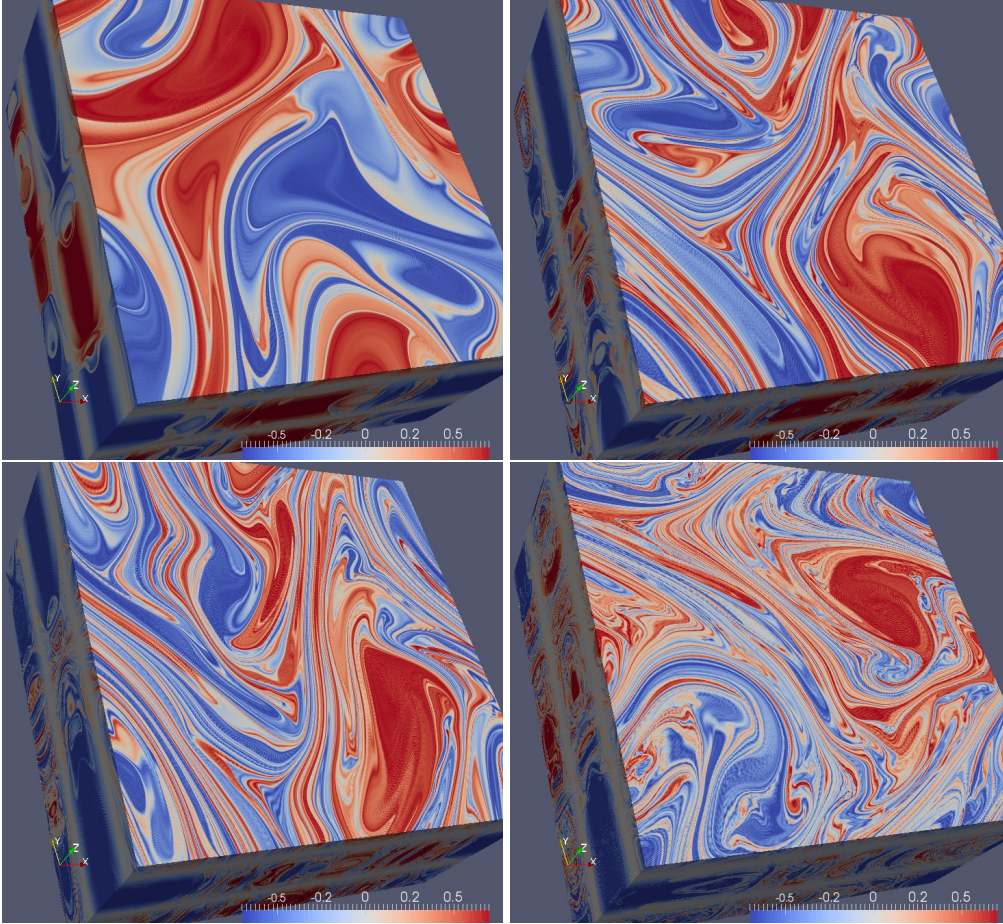


FIGURE 7. Snapshots of perturbation potential vorticity in the QG system. The times of the snapshots are close to the time of: top-left: the local peak in Ro_ω around 4.8; top-right: global minimum of $A - S$ around 6.1; bottom-left: global minimum of Ro_ω and global maximum of Fr_ω near 6.4; bottom-right: global maximum of Ro_ω , around 7.0.

in the base flow, the structure and scale of these baroclinic modes are not immediately apparent; linear stability analysis that is ongoing is likely to shed more light on these aspects. The progressive destabilization of small scales can also be seen in the plot of spectral flux of energy at different times in Fig. 8. However, and as expected, all of these instabilities only lead to an inverse cascade. Additionally, we have previously seen that the QG approximation tends to be inapplicable in at least some isolated regions of the flow domain beyond times as early as 2.5. While isolating such regions and examining dynamics in their vicinity could lead to further insight, we have not attempted this yet.

4.3. Front Formation in the Boussinesq System

As mentioned in the previous subsection, there is general similarity in the initial evolution of the Boussinesq system to that in the QG system. Past time 2.5, however, evolution of the two systems differ significantly and this is evident in previously presented diagnostics such as those in Figs. 3, 4, and 5. Indeed a striking difference in the evolution of the Boussinesq system as compared to that of the QG system is the spatially-localized event around time 4.8 (starting at about time 4.5 and ending at about time 5.1) seen in Fig. 4

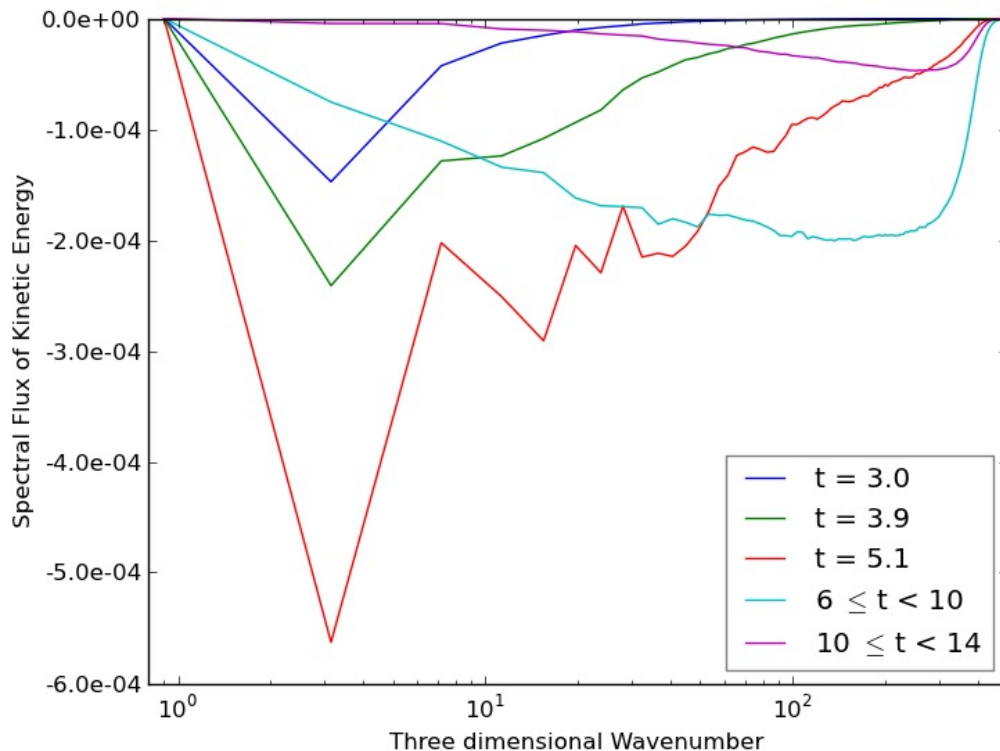


FIGURE 8. A plot of the nonlinear spectral flux of kinetic energy as a function of three-dimensional wavenumber in the QG 2x case. Three instantaneous plots over the early period and two time-averaged plots over intermediate and late times are shown. A progressive destabilization of small scales is seen. All instabilities, however, lead to an inverse cascade of kinetic energy.

when peak vorticity-based Rossby and Froude numbers briefly reach large values. This event is not seen in the domain-averaged measures such as in Fig. 3. It is possible that this event is related to the formation of steep fronts by mesoscale shearing and straining. To further explore this possibility, Fig. 9 shows buoyancy spectra at times 2.4, 3.6, 4.5, and 6.0 for the quasi-geostrophic system and the Boussinesq system in the main panel. The fall-off of the spectra in the quasi-geostrophic system is seen to be close to the expected -5 scaling. The spectra of the Boussinesq system (at $t > 2.4$) are seen to be steeper. Indeed, their slope is seen to be close to -2 , as would be expected with the formation of fronts, and somewhat shallower than the $-8/3$ slope obtained by Andrews & Hoskins (1978) using semigeostrophic theory (For why the spectral slope tends to more often be closer to -2 than $-8/3$, see Boyd (1992).)

Next, compare the difference in the spectra at small scales in the two systems between times 2.4 and 3.6. The accumulation of energy at small scales is seen to be significantly faster in the Boussinesq system than in the QG system. This is most likely related to the influence of ageostrophic circulation of the time scale for frontogenesis (Holton *et al.* 2004). This influence in the Boussinesq system is like in the semigeostrophic system that is typically used for analyzing frontogenesis (e.g., see Holton *et al.* 2004). This influence leads to a positive feedback in the growth of horizontal density gradients because an increase in the horizontal density gradient leads to an increase in the strength of the secondary ageostrophic circulation which in turn accelerates the growth of horizontal density gradient. However, in the QG system, with only the geostrophic circulation driving the

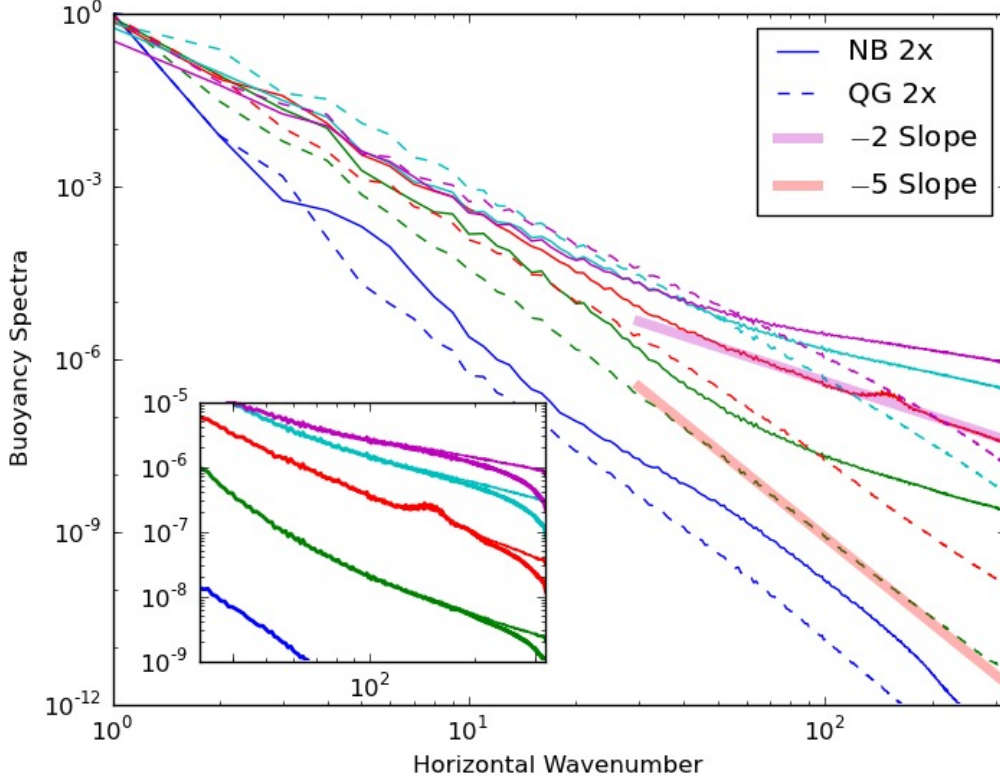


FIGURE 9. Buoyancy spectrum is shown as a function of horizontal wavenumber for the QG and Boussinesq systems at times 2.4 (blue), 3.6 (green), 4.5 (red), 6.0 (cyan), and 8.0 (magenta). Spectral slopes past time 2.4 are steeper in the Boussinesq system than in the QG system suggesting occurrence of fronts in the Boussinesq system. Slopes close to -2 are seen at some of the intermediate times such as seen here at time 4.5. Close spacing of spectra at times 6 and 8 suggest a slowdown in frontogenesis past a time of about 6. The inset plot shows that there are minor changes to the spectra at wavenumbers smaller than about 200 when hyperviscosity and hyperdiffusivity coefficients in the horizontal are increased by a factor of 10.

increase in horizontal density gradient, this feedback is absent and the resulting rate of growth in horizontal density gradient is smaller. Further, since the formation of fronts is likely an important process in the chain of events leading to dissipation of balanced mesoscale energy, the dependence of the buoyancy spectra shown in the main panel for the Boussinesq system to a change in the coefficient of small-scale dissipation parameterization is shown in the inset. In this inset, the thicker lines correspond to a case where the coefficient of horizontal hyperviscosity and hyperdiffusivity have been increased by a factor of 10. Changes to spectra at wavenumbers smaller than about 200 are seen to be minimal.

Figure 10 shows the horizontal gradient of buoyancy at time 4.5 when a local peak in the buoyancy spectrum is seen in Fig. 9 at a horizontal wavenumber of about 150. The $x - y$ plane corresponds to the top surface in Figs. 1, 2, and 7. The left panel shows the full $x - y$ plane and the right panel shows a zoom of the region marked by the rectangle in the left panel. Elongated frontal features with narrow cross-frontal widths seen in this figure are likely regions of enhanced unbalanced instabilities. We also note that regions of strong horizontal density gradients did not preferably coincide with regions of either

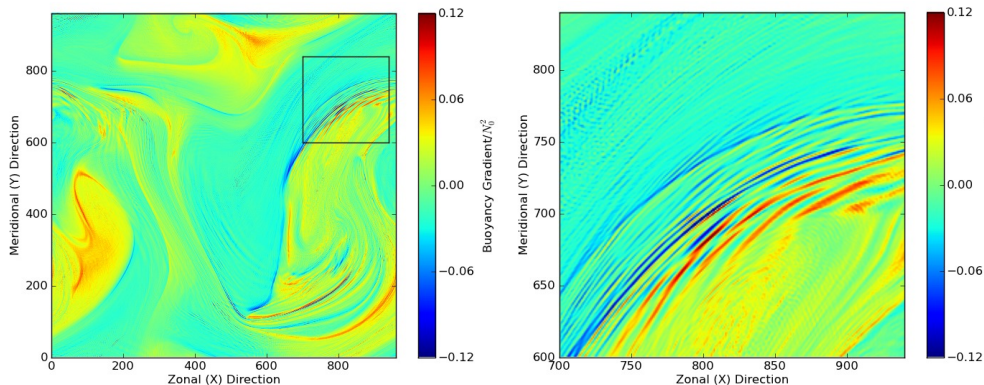


FIGURE 10. Magnitude of the horizontal gradient of buoyancy on an $x - y$ plane at time 4.5. The full $x - y$ domain is shown on the left. A zoom of the region marked by the square is shown on the right. The $x - y$ plane corresponds to the top surface in Figs. 1, 2, and 7

weak or strong stratification (e.g., see Fig. 13). leading to an irreversible forward cascade of energy. While further investigation of the secondary ageostrophic circulation in the cross-frontal plane may be possible, for example by using the Sawyer-Eliassen equation, the curved nature of the fronts makes this task difficult.

4.4. Inertial and Symmetric Instability

We now consider the possibility of inertial and symmetric instabilities occurring in the Boussinesq system. To this end, we briefly consider the dynamics of potential vorticity following Thomas *et al.* (2013). For this purpose, it is useful to consider potential vorticity as a combination of two terms, the first of which comprises terms involving the vertical component of absolute vorticity (and/or vertical gradients of buoyancy) whereas the second comprises terms involving the horizontal component of vorticity (and/or horizontal gradients of buoyancy). For this purpose, (3.4) may therefore be rewritten as

$$Q = Q_{vert} + Q_{bc} = (1 + Ro\zeta) \left(1 + Fr \frac{\partial b}{\partial z} \right) + \boldsymbol{\omega}_h \cdot \nabla_h b. \quad (4.5)$$

Dimensionally this corresponds to $Q^{(d)} = Q_{vert}^{(d)} + Q_{bc}^{(d)} = \zeta_a^{(d)} N^2 + \boldsymbol{\omega}_h^{(d)} \cdot \nabla_h^{(d)} b^{(d)}$, where ζ_a is the vertical component of (dimensional) absolute vorticity.

When the sign of potential vorticity is the opposite of that of the Coriolis parameter, the flow is unstable to overturning instabilities (Hoskins 1974). Since these arguments are more intuitive and traditional in the dimensional form, we will use that and the corresponding nondimensional form will be indicated in parentheses. (Referring to (4.5), the above condition occurs when $Q < 0$.)

The main cause for low (negative) potential vorticity can be associated with vertical vorticity (first term on the RHS), stratification (second part of first term) or baroclinicity of the flow (last term).

a) When $N^2 < 0$ ($1 + Fr \partial b / \partial z < 0$), the instability is the gravitational instability—an instability to vertical displacement of a fluid particle.

b) When $N^2 > 0$, but $f \zeta_a N^2 < 0$ ($1 + Fr \partial b / \partial z > 0$, but $(1 + Ro\zeta) (1 + Fr \partial b / \partial z) < 0$) the resulting instabilities are termed inertial or centrifugal instabilities—an instability to horizontal displacement of a fluid particle.

c) When $N^2 > 0$ and $f \zeta_a N^2 > 0$, but $f q < 0$, the resulting instabilities are termed

symmetric instabilities—an instability to a slantwise displacement of a fluid particle, also thought of as an isopycnal inertial instability.

Thus for symmetric instability to occur, $Q_{bc} < 0$ and $|Q_{bc}| > |Q_{vert}|$, indicating that symmetric instability is associated with strong baroclinicity. To consider this case further, we note from scale analysis that the horizontal component of vorticity is well approximated by

$$\boldsymbol{\omega}_h \approx \left(-\frac{\partial v}{\partial z} \hat{\mathbf{x}}, \frac{\partial u}{\partial z} \hat{\mathbf{y}} \right).$$

Consequently, the second term of (4.5) can be approximated as

$$Q_{bc} \approx \frac{\partial u}{\partial z} \frac{\partial b}{\partial y} - \frac{\partial v}{\partial z} \frac{\partial b}{\partial x}.$$

For a flow in thermal wind balance, this reduces to

$$Q_{bc}^g = -\frac{1}{f} |\nabla_h b|^2,$$

showing that baroclinicity results in lowering potential vorticity (Thomas *et al.* 2013). However, in an unbalanced flow, baroclinicity could act to either decrease or increase potential vorticity.

We consider related diagnostics in Fig. 11. In this figure, the minimum of potential vorticity, minimum of stratification, minimum of the Q_{vert} , and the maximum of $|Q_{bc}|/Q_{vert}$ are shown as a function of time. For the first of these three diagnostics, the minimum over the full domain is considered. However, for the last of the diagnostic, the maximum is considered over the part of the domain where $Q_{bc} < 0$, for the reason that Q_{bc} can be positive in an unbalanced flow. The y -axis for the first of these diagnostics is on the left where as that for the last is on the right side and a logarithmic scale is used. A reference line at $y = 0$ for the first three of the diagnostics and a reference line at $y = 1$ for the last diagnostic are shown. A yellow stick is shown to highlight the first time potential vorticity becomes negative in the flow (at $t \approx 4.5$ at the right end of the stick) and the time preceding it (at $t \approx 4.2$ at the left end of the stick).

At initial times minimum of Q is coincident with the minimum of Q_{vert} , the flow is stably stratified everywhere, and the maximum of $|Q_{bc}|/Q_{vert}$ where $Q_{bc} < 0$ is less than unity. Consider the state of the system at time 4.2 on the left side of yellow stick. At this time, when for the first time, minima of Q and Q_{vert} are not coincident, two conditions seem imminent: a) Q_{vert} is tending to go negative, and b) the magnitude of Q_{bc} is tending to exceed the value of Q_{vert} in a region where $Q_{bc} < 0$ and $Q_{vert} > 0$. These are exactly the conditions for a) inertial/centrifugal instability and b) symmetric instability respectively.

Indeed at time 4.5 on the right side of the yellow stick, potential vorticity has become negative for the first time and both of the above conditions are seen to be satisfied (in separate regions), suggesting that the flow is susceptible to both inertial/centrifugal instability and symmetric instability. To verify this further, we consider points in the domain at time 4.5 where $Q < 0$. At each of these points, we plot the values of Q_{vert} , Q_{bc} , stratification, and the ratio Q_{bc}/Q_{vert} ; the last of these is shown in an inset plot. The nearly-diagonal distribution of Q_{vert} vs. Q implies that Q becoming negative is largely due to Q_{vert} becoming negative. That is, conditions for inertial/centrifugal instability are satisfied.

Nevertheless, in regions where potential vorticity takes on small negative values, it is seen that there are points with $Q_{vert} > 0$. Further, at these points, $Q_{bc} < 0$ and the magnitude of Q_{bc} exceeds that of Q_{vert} leading to conditions that satisfy the necessary

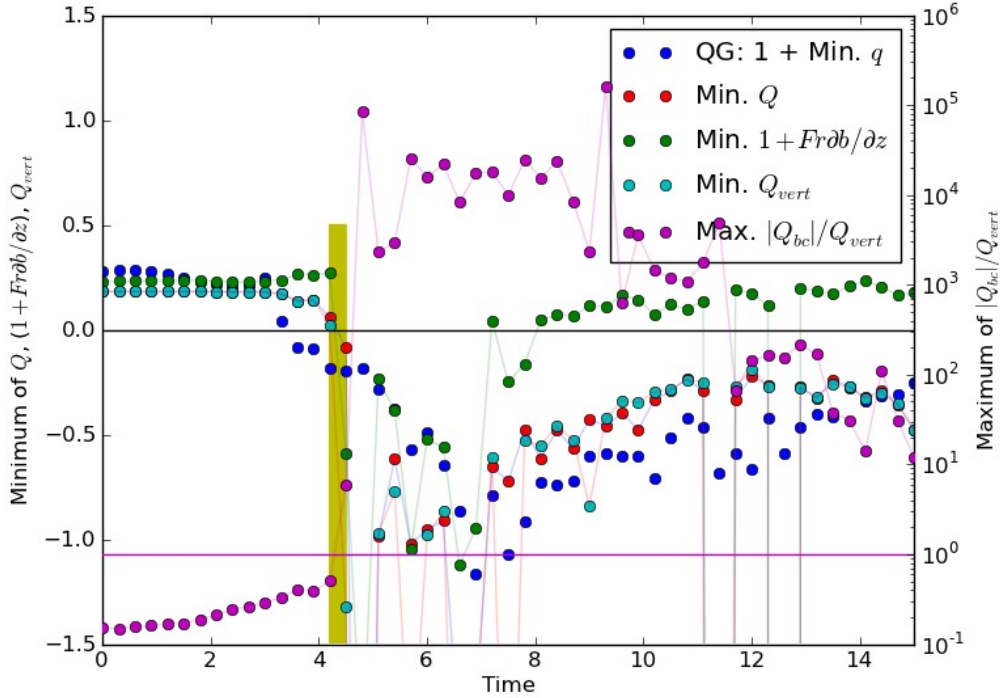


FIGURE 11. Evolution of three (Ertel) potential vorticity related diagnostics are plotted as a function of time of the NB 2x case. These are the minimum value of potential vorticity in red, minimum value of the vertical component of potential vorticity as given by the first term on the RHS of (4.5) in cyan and the maximum value of the ratio of the absolute value of the baroclinic component of potential vorticity as given by the second term on the RHS of (4.5) and the vertical component (logarithmic scale on right) in magenta. Also shown are the the minimum of potential vorticity for the QG 2x case in blue and the minimum of stratification for case NB 2x in green. The yellow stick is placed to facilitate seeing the values of these terms just before (left edge of stick) and just after (right edge) the minimum value of potential vorticity becomes negative in case NB 2x. A black horizontal line is drawn at the zero of the y -axis on the left and a horizontal line in magenta is drawn at at $y = 1$ for the y -axis on the right. Conditions for both inertial instability and symmetric instability are seen to be satisfied first at time 4.5 and other subsequent times.

condition for symmetric instability. Further, an examination of these diagnostics at subsequent times in conjunction with those in Fig. 11 show that the conditions for these instabilities are met over an extended period of time.

The diagnostics in the previous section and this one then suggest the following picture: Following the formation of mesoscale eddies by hydrostatic geostrophic baroclinic instability, mesoscale shear and strain drive the formation of fronts. Steep fronts first form at a time of about 4.5. Potential vorticity becomes negative for the first time at about the same time (hand in hand). Thus, concurrent with the formation of fronts, necessary conditions for inertial and symmetric instabilities are also satisfied for the first time. These conditions continue to be satisfied over most of the remainder of the time we consider evolution over, whereas frontogenesis slows down beyond a time of about 6.

Figure 13 shows regions of negative potential vorticity at four times starting at time 4.5 when the minimum of potential vorticity first becomes negative to time 6.2 when the fraction of the domain where potential vorticity is negative reaches its peak value of about 0.03% (see Fig. 6). The two intermediate times are 5.1 and 5.7. This figure shows

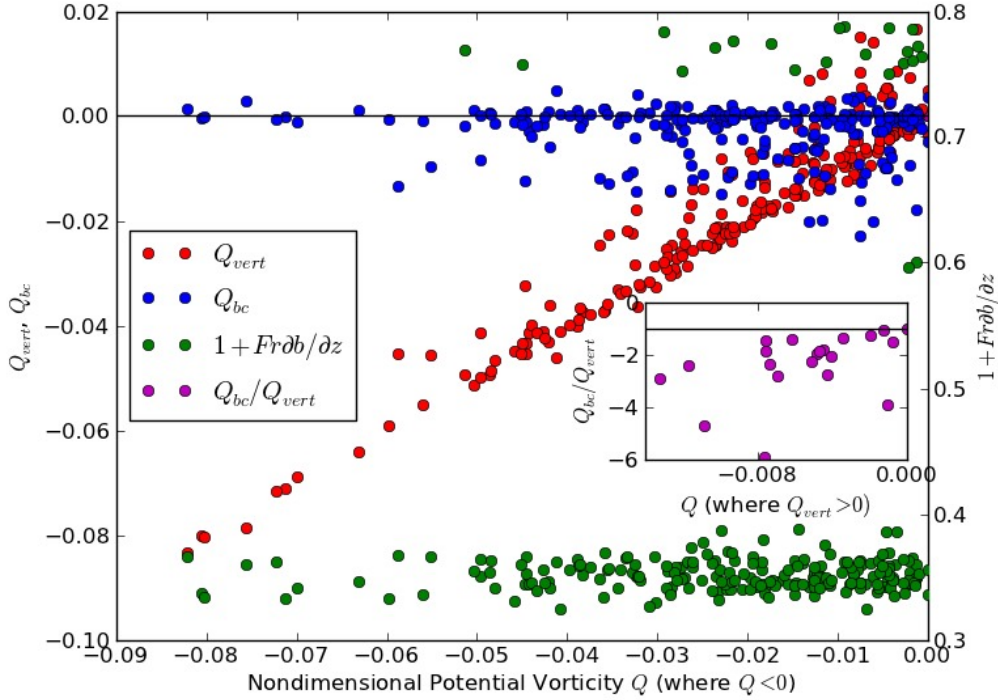


FIGURE 12. Potential vorticity diagnostics at time 4.5 and at locations where $Q < 0$. At each of these points, values of Q_{vert} , Q_{bc} , stratification, and the ratio Q_{bc}/Q_{vert} are plotted against potential vorticity; the last of these is shown in an inset plot. At points where $Q_{vert} < 0$ in the main panel conditions for inertial instability are met. At points where $Q_{bc}/Q_{vert} < 0$ in the inset plot, conditions for symmetric instability are satisfied.

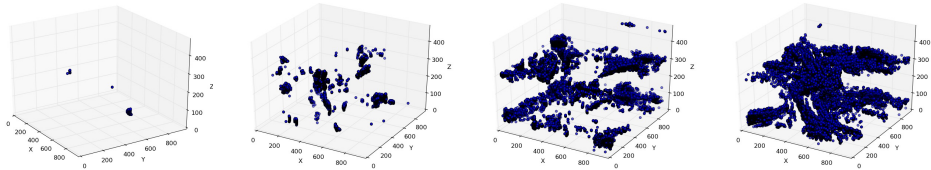


FIGURE 13. Regions with negative potential vorticity are shown from start of instability at time 4.5 to a time of 6.2, when the fraction of domain with negative potential vorticity peaks. Intermediate times shown are 5.1 and 5.7. The volume of domain where potential vorticity is negative is highly exaggerated—at time 6.2, the region of negative potential vorticity occupies about 0.03% of the total domain.

that even though the fraction of the domain where fronts and unbalanced instabilities occur are small, they are not localized, but rather well spread out in the domain.

4.5. Potential Vorticity Snapshots in the Boussinesq System

Like with the QG system, Fig. 14 shows four snapshots of Ertel potential vorticity in the Boussinesq system.

The times of the snapshots are chosen to be close to the time of the local peak in Ro_ω around 4.5 in Fig. 4 (top-left), local minimum of Ro_ω and the local minimum of $A - S$ around 6.6 in Figs. 4 and 5 respectively (top-right), local maximum of Ro_ω near 8.1 in Fig. 4 (bottom-left), and at the late time of 15 (bottom-right).

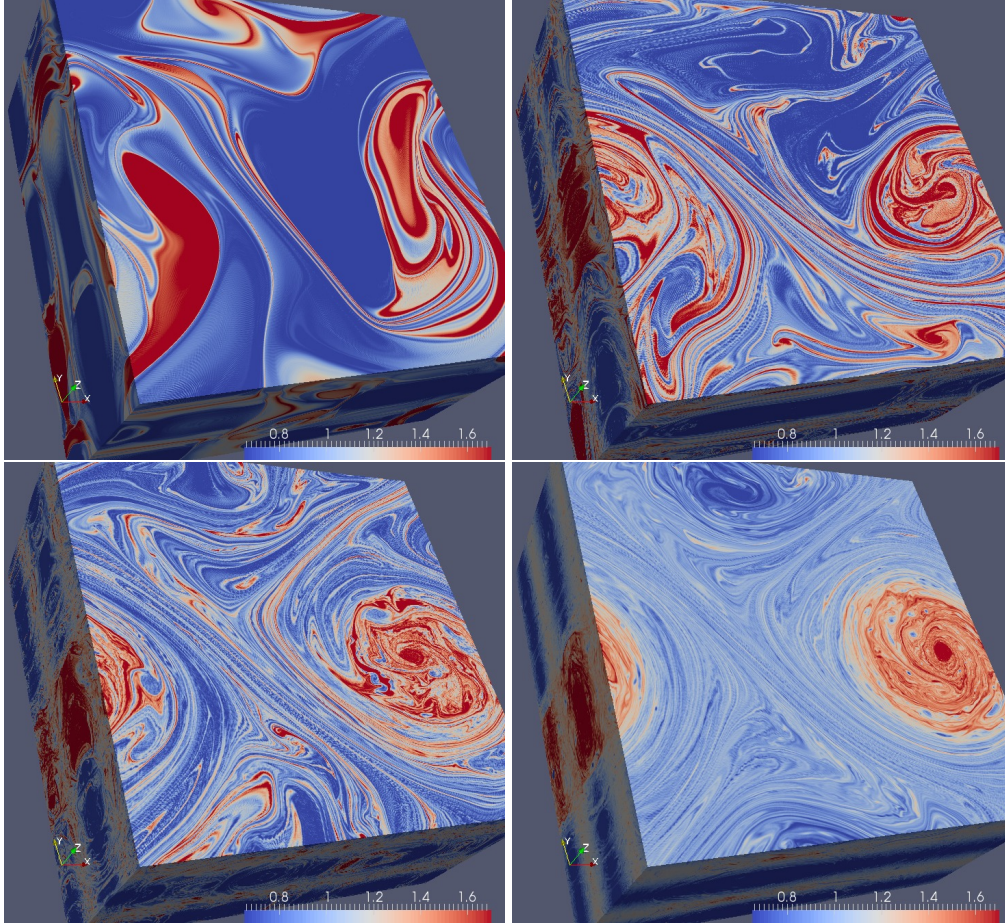


FIGURE 14. Snapshots of potential vorticity in the Boussinesq system. The times of the snapshots are close to the time of: top-left: the local peak in Ro_ω around 4.5; top-right: local minimum of Ro_ω and the local minimum of $A - S$ around 6.6; bottom-left: local maximum of Ro_ω near 8.1; bottom-right: at the late time of 15.

The times of the four snapshots are chosen as follows: The time of the snapshot in figure 14(a) corresponds to the time of the local peak in Ro_ω in figure 4 near time 4.5. The snapshot in figure 14(b) is at a time 6.6, a time close when a local minimum of Ro_ω occurs in figure 4 and a local minimum of $A - S$ occurs in figure 5. That in figure 14(c) is at a time 8.1, around which a local maximum of Ro_ω occurs in figure 4. Finally, the snapshot in figure 14(d) is at the late time of 15.

The similarity in the phenomenology of the large scales noted earlier is reflected in the gross similarity of the large-scale features in Fig. 14 and 7. The most noticeable difference between the two figures, however, is that small horizontal scales are more energetic in the Boussinesq system. This is consistent with the phenomenology presented previously that include the ready formation of fronts and further susceptibility of these frontal regions to imbalanced instabilities in the Boussinesq system.

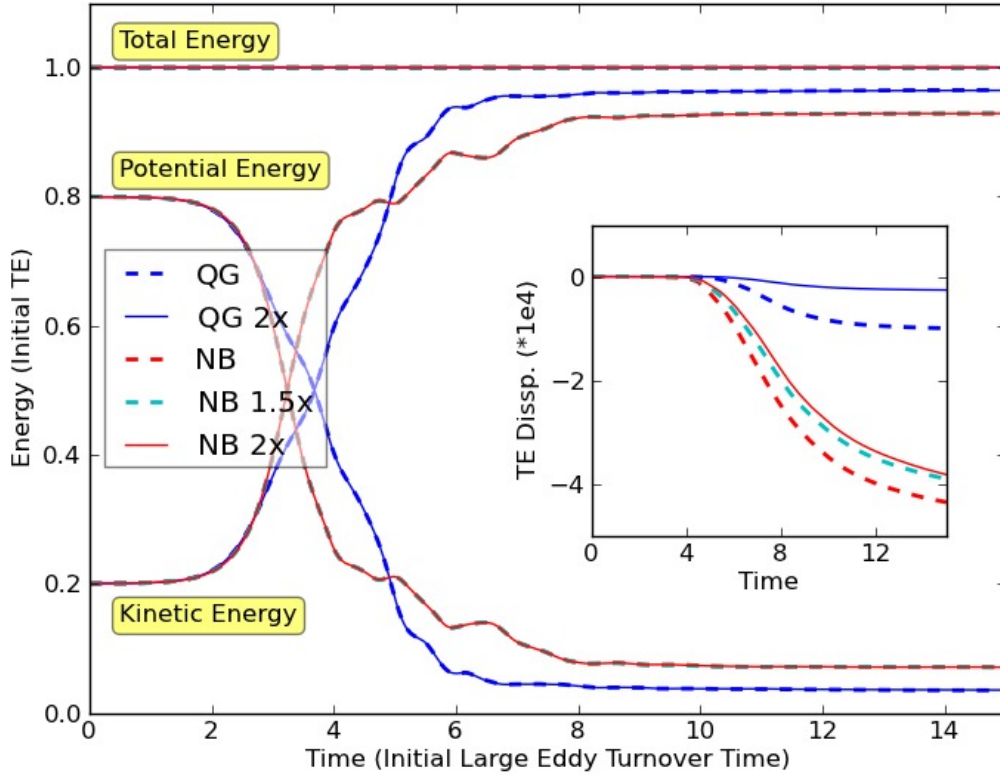


FIGURE 15. Evolution of kinetic, potential and total energy in the reference run in the quasi-geostrophic and Boussinesq systems at two different resolutions. While early development in the two systems are similar (up to about time 5), later development is seen to be different with a marked slowdown in the conversion from potential energy to kinetic energy in the Boussinesq system. The main effect of resolution is seen in the dissipation of total energy, as shown in the inset plot. In this inset plot, dissipation of total energy is shown in hundredths of a percent of total energy.

5. Scaling of Dissipation with Rossby number

We first consider dissipation in the reference simulation. The main panel of Fig. 15 shows the evolution of kinetic, potential, and total energy at two resolutions (1x and 2x) in the QG system and at three resolutions (1x, 1.5x, and 2x) in the Boussinesq system for the reference case. The inset shows the evolution of total energy on a highly magnified scale. The initial growth of the baroclinic instability is seen to be similar in the two systems and at the different resolutions (main panel). At about four eddy turnover times, while baroclinic instability has already resulted in the conversion of a large fraction of the available potential energy into kinetic energy (main panel), total energy is seen to be very weakly dissipated (inset).

In the main panel of Fig. 15, kinetic and potential energy evolution is seen to depend only rather weakly on resolution. This is, however, not the case with total energy or equivalently its dissipation shown in the inset plot. The vertical axis of the inset plot corresponds to dissipation in terms of a hundredth of a percent of the initial total energy. Although the level of dissipation is seen to depend on resolution in both systems, in terms of fractional change, this dependence is much stronger in the QG system. Indeed, dissipation in the QG system is verified to approach zero using Richardson’s deferred

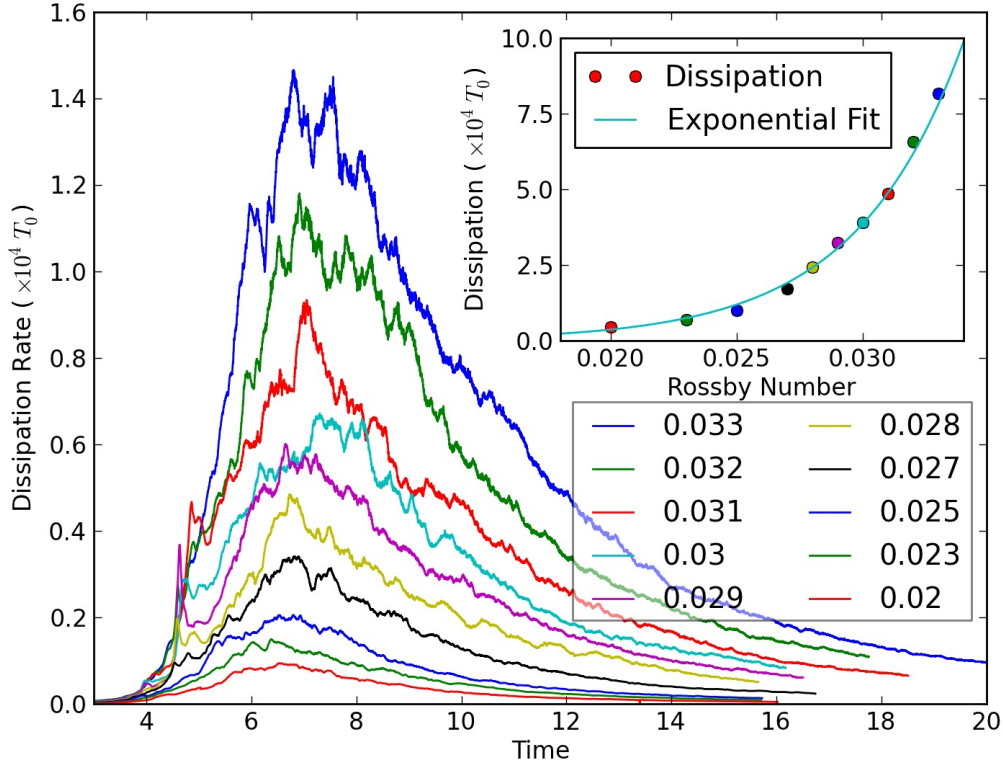


FIGURE 16. Main panel: Dissipation rate as a function of time at various Rossby numbers. Corresponding Rossby numbers are shown in the legend. Cumulative dissipation at time 15.7 is plotted as a function of Rossby number using the same colored circles in the inset. The continuous line in the inset corresponds to a least-squares exponential fit of the dissipation values.

approach to the limit of infinite resolution. In the Boussinesq system, dissipation is seen to approach a finite value. Next we quantify the dependence of this value on Rossby number.

5.1. Scaling with Rossby Number

As mentioned previously, one of the main motivations for this work is to examine the energetic consequences of imbalanced instabilities in the interior. In the previous section, it was seen that dissipation of total energy in the quasi-geostrophic approximation displayed the familiar vanishing behavior whereas that in the Boussinesq system, it approached a finite value with increasing resolution. In this section, we examine how dissipation in the Boussinesq system varies with Rossby number.

To this end, we varied the velocity-based Rossby number of the initial condition over a range of values in nine other 'NB 2x' experiments. We note here, that in order to preserve similarity in the initial evolution between the quasi-geostrophic and Boussinesq systems (as seen in the previous section), the ratio of the Froude number to Rossby number was held fixed at its value (of two) in the reference run.

The main panel of Fig. 16 shows the time evolution of the rate of dissipation of total energy in the main sequence of 'NB 2x' runs. The legend indicates the Rossby number of the corresponding profiles. (It is hoped that the ambiguity in line type is not a cause for confusion.) These curves are seen to display a characteristic asymmetry in that the

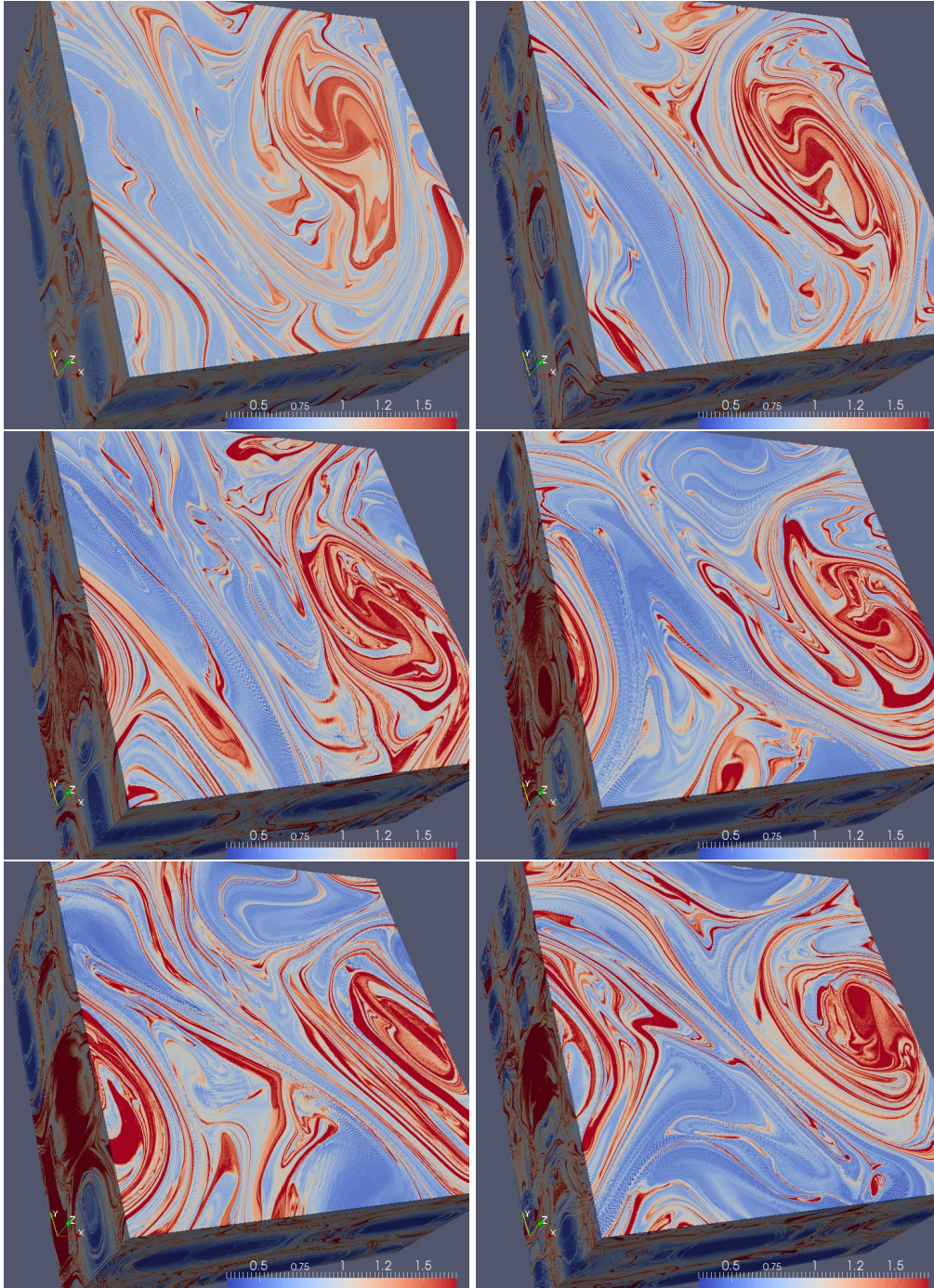


FIGURE 17. Snapshots of the potential vorticity field at time 6 in six of the ten Boussinesq cases considered in Fig. 16. Rossby numbers of 0.02, 0.025, 0.029, 0.03, 0.031, and 0.033 going from top-left to bottom-right. At this time, dissipation rate is seen to be close to peak values, but dissipation rate is still rising. Frontogenetic processes are likely still active.

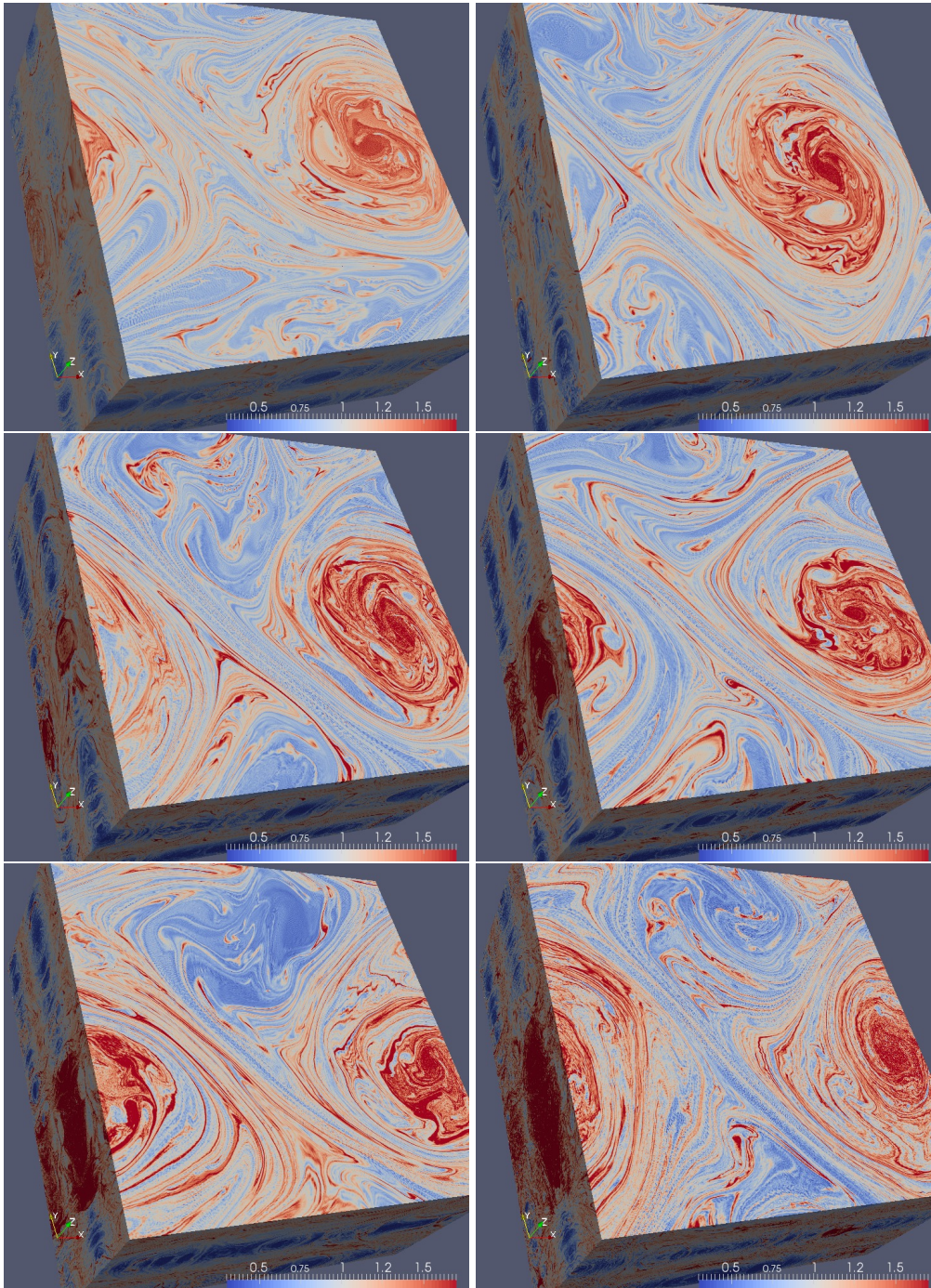


FIGURE 18. Same as if Fig. 17 but at a later time of 8 when dissipation rate is decreasing. Absence or reduced frontogenesis and increased break-up of fronts by imbalanced secondary instabilities is the likely reason for qualitative differences from Fig. 17.

rise in the dissipation rate between times 4 and about 7 is steeper than the fall from the peak. As discussed in the previous section, the steeper rise is due to frontogenesis being active over that period. Indeed, a slow down in the formation of fronts is the cause for the peak.

In the inset plot in Fig. 16, the total dissipation at time 15.7 is plotted as a function of Rossby number for each of the experiments. The least squares exponential fit is drawn as a continuous line and it is seen to be a good fit. In order to rule out the possibility of numerical artifacts contributing to the exponential scaling, the 'QG 1x' series of experiments over the range of Rossby number from 0.02 to 0.03 were analyzed in an identical fashion. While cumulative dissipation in the Boussinesq system (as seen in the inset plot Fig. 16) varied by about a factor of 10 over this range of Rossby numbers, the variation in the QG system was about 0.1%: In the inset plot, QG dissipation as a function of Rossby number would be visually indistinguishable from a horizontal line. These comparisons suggest that numerical artifacts contribute minimally to the exponential increase of dissipation with Rossby number in the Boussinesq system.

Figures 17 and 18 show snapshots of potential vorticity at times close to 6 and 8 respectively in six of the ten cases considered in Fig. 16 (Rossby numbers of 0.02, 0.025, 0.029, 0.03, 0.031, and 0.033 going from top-left to bottom-right). Both these times are times when dissipation rate is seen to be high and in fact close to peak values in Fig. 16. On this count it would seem surprising that the fields are qualitatively quite different at the two times. However, at time 6 dissipation rate is still rising unlike at time 8 when dissipation rate is on its way down. Indeed, one of the main difference in the potential vorticity fields at these two times is that the elongated filamentary structures are more coherent at time 6 than they are at time 8. A plausible explanation of this difference is that the faster rise in dissipation rate in Fig. 16 is in part due to the forward cascade of energy associated with the formation of fronts. Note that this is a statistical statement about the overall state of the flow considering that the timescale for the formation of fronts is likely much shorter than a large-scale eddy turnover time. On the other hand, a slower fall-off in the dissipation rate past a time of about 7 is likely due to an absence or at least a reduced rate of formation of fronts; the main processes that underlie dissipation during this phase are the secondary imbalanced instabilities. We will present further evidence to support this explanation in the next section when we discuss nonlinear spectral flux of energy across scale.

6. Spectral Scaling and Spectral Flux of Energy Across Scale

We now examine spectral scaling of total energy as a tool to diagnose imbalance. In the main panel of Fig. 19, spectra of total energy are plotted as a function of the three dimensional wavenumber after scaling the vertical by N/f . In the inset plots, distribution of total energy with horizontal and scaled vertical wavenumbers are plotted; the vertical spectra in the inset are offset by a decade and a half for ease of presentation. The horizontal axis in the inset plot spans the same range of scales as in the main panel and is omitted to reduce clutter. The QG and Boussinesq cases compared in previous diagnostics ($Ro = 0.03$) are shown in heavy lines, with the QG case shown in blue, and the Boussinesq case in red. The dashed lines correspond to series of Boussinesq cases with Ro ranging from 0.02 to 0.033. Recalling that the energy spectrum in the balanced regime of forward potential enstrophy cascade scales as -3 , this slope is shown for reference. It is seen in this plot that the intermediate range of scales (wavenumber less than about 30) in all the Boussinesq cases and most of the scales in the QG 2x case display the balanced -3 scaling. The slightly steeper fall-off at small scales in QG 2x is not unusual

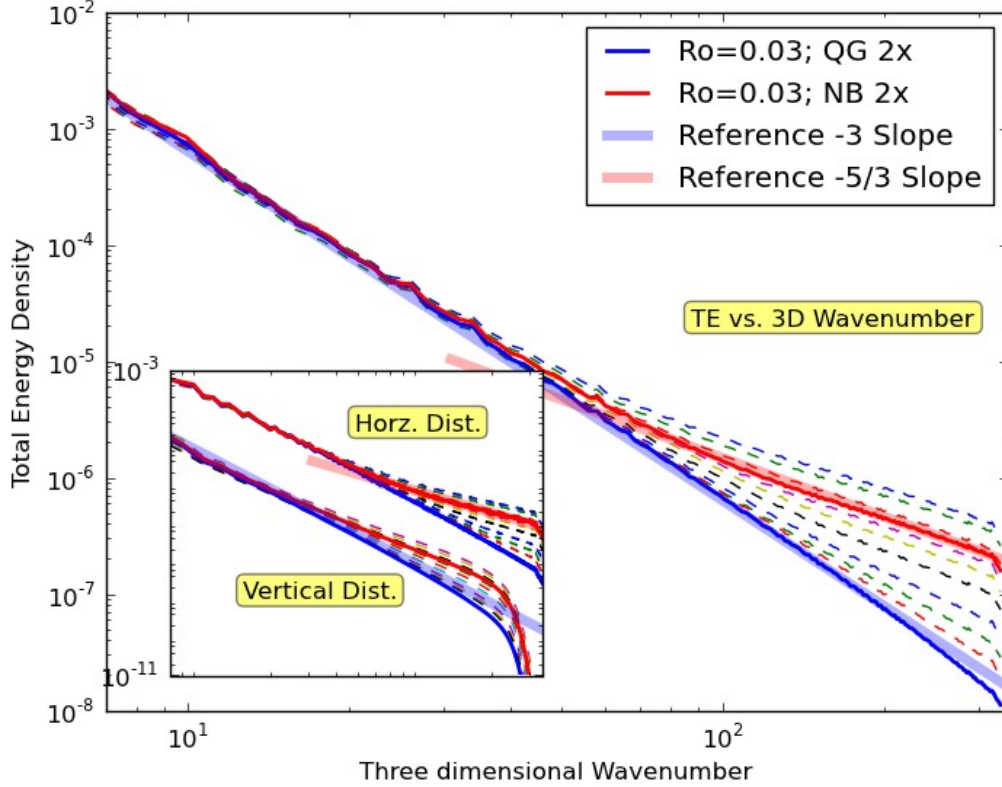


FIGURE 19. Total energy spectra in the QG and Boussinesq systems with 2x resolution. The cases considered in detail in previous diagnostics ($Ro = 0.03$) are shown in heavy lines: blue: QG, red: Boussinesq. The dashed lines correspond to Boussinesq cases with Ro ranging from 0.02 to 0.033. In the main panel, spectra are plotted against the three dimensional wavenumber where the vertical is scaled by N/f . In the inset, spectra are plotted against the horizontal wavenumber for the top set of curves and against the vertical wavenumber (scaled by N/f) for the lower set of curves. Spectra are averaged between times 5 and 13 A shallowing of the spectra from the -3 quasi-geostrophic scaling is seen over an increasing range of small scales at Ro is increased.

and has been previously noted in many instances; it is thought to be related in part to the existence of coherent structures.

In the Boussinesq system, it is seen that as Ro increases, there is an increasing range of small scales where the spectrum displays a shallower fall off. Processes that lead to deviations from a balanced regime and which have the potential to lead to a forward cascade of energy are expected to lead to shallower spectral slopes (e.g., see Bartello 1995). However, the exact dynamics associated with this shallower fall-off is a topic of debate and an area of on-going research. For example, it has been suggested that when rotational control is reduced at small scales, there is likely to be a regime of anisotropic stratified turbulence before a regime of more isotropic turbulence is realized at yet smaller scales. For example, Lindborg and co-workers (Lindborg 2006; Riley & Lindborg 2008) suggest that the kinetic and potential energy spectra each scale as $k_h^{-5/3}$ in the horizontal and k_z^{-3} in the vertical in the regime of stratified turbulence where energy cascades forward. While their scaling in the horizontal is the same as in the regime of isotropic three-dimensional turbulence where energy cascades forward as well, anisotropy of dy-

namics in the stratified regime leads to a steeper fall-off of the energy spectrum in the vertical. For this reason, a reference $-5/3$ slope is indicated on the three-dimensional wavenumber distribution and horizontal wavenumber distribution plots. Indeed, at small scales, the spectra of total energy against the three-dimensional wavenumber and the horizontal wavenumber is seen to match this slope over an increasing range of scales for increasing Rossby number. We expect that with yet higher resolutions, the lower Rossby number cases will also display shallower spectra over a larger range of scales than seen with the present resolution.

6.1. Vertical Shear Spectrum and Stratified Turbulence

The spectral fall-off of the total energy spectrum with vertical wavenumber is seen to be shallower than the -3 spectral fall-off of stratified turbulence (Lindborg 2006). At first glance, this suggests that a regime of stratified turbulence that is presumably fed by imbalanced instabilities is not clearly realized in these simulations. However, as mentioned earlier, the spectra in Fig. 19 are averaged between times 5 and 13 which spans different regimes from the point of view of stratified turbulence.

We examine further if indeed the simulations are entering a regime of stratified turbulence. To this end, we note that from Fig. 3 (where the rms value of Fr_ω becomes small at late times) and from the inset plot in Fig. 4 (where the peak value of Fr_ω is smallest, again at late times), stratified turbulence, if realized, is most likely to occur at late times. Consequently, Fig. 20 shows the spectral distribution of the vertical shear of horizontal velocity as a function of vertical wavenumber in all the cases considered. A minimum in this spectrum, occurring in the vicinity of the wavenumber corresponding to the Ozmidov scale, is interpreted as indicative of a transition between those scales of motion that are strongly influenced by stratification and those that are not (Riley & Lindborg 2008).

A minimum is indeed seen in these spectra in Fig. 20 at late times for the higher of the Rossby numbers considered and occurs between wavenumbers 100 and 200. Further, the spectra in Fig. 20 are qualitatively similar to those in Fig. 1 of Gargett *et al.* (1981) which is a composite based on in-situ measurements. (This latter figure is reproduced and discussed in Riley & Lindborg (2008).) Nevertheless, further detailed investigation is necessary to assess the relevance of these simulations to the in-situ measurements of Gargett *et al.* (1981).

It is also clear that a minimum is not seen in Fig. 20 for the smaller of the Rossby numbers considered. This transition as a function of Rossby number from having a minimum to not having one is rather continuous, with the minimum becoming shallow before disappearing. Which leads us to suggest that the question is not one of whether or not stratified turbulence spans the regimes of anisotropic rotating-stratified turbulence at large scales and more isotropic turbulence at small scales, but one of how important it is in the particular case or parameter regime of interest.

6.2. Spectral Flux of Energy Across Scale

We first present an overall picture of the flow evolution in terms of the spectral flux of kinetic energy (KE), available potential energy (APE) and total energy (TE) across scale. To this end, Fig. 21 shows the spectral flux across scale of KE \mathcal{K}_{tr} (blue), that of APE \mathcal{P}_{tr} (cyan), and that of TE \mathcal{T}_{tr} as a function of the three-dimensional wavenumber (see Section 3.3 and details around (3.8)). Averages over four time periods are shown.

Between times 2 and 4 the hydrostatic geostrophic baroclinic instability is in its nonlinear phase mesoscale eddies are being formed. In this phase, the expected forward cascade of APE is clearly seen. As for the spectral flux of KE, two processes are at play. First, note

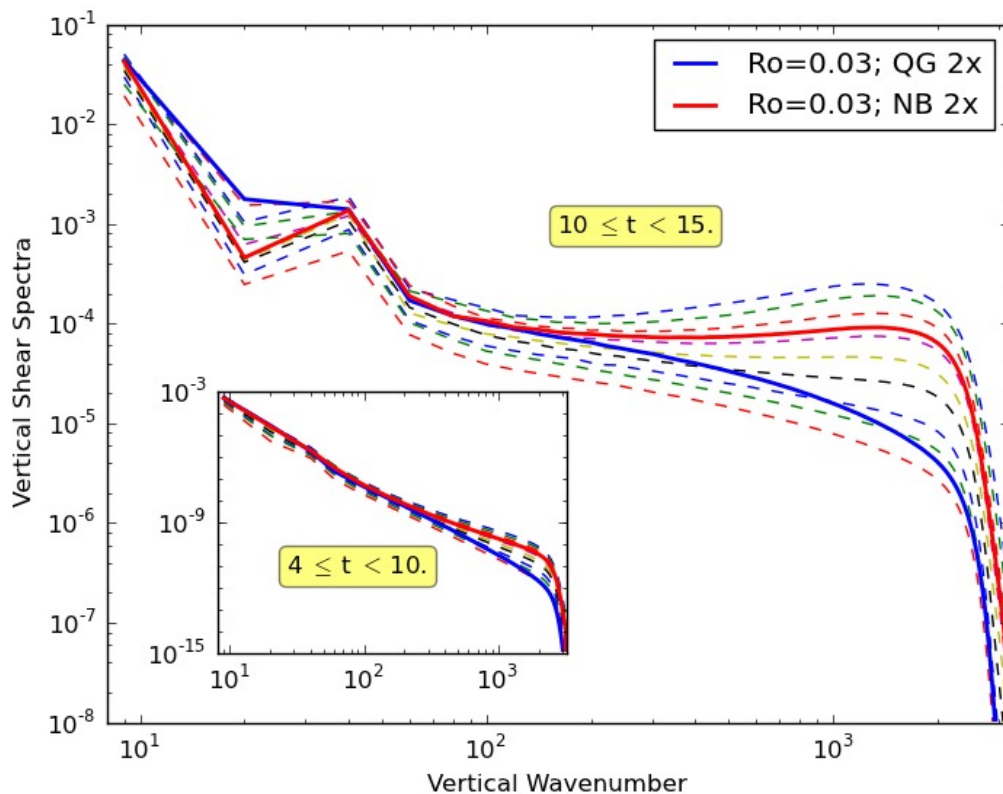


FIGURE 20. Spectrum of vertical shear of horizontal velocity as a function of vertical wavenumber for the main sequence of 2x cases considered. Main panel shows the average over late times whereas the inset shows the average over intermediate times. A minimum in this spectrum, seen here at late times for the larger of the Rossby numbers considered, is indicative of a transition from anisotropic stratified turbulence to more isotropic turbulence. A similarity of this figure to Fig. 1 of Gargett *et al.* (1981) which is a composite based on in-situ measurements is noted.

that that initial KE is concentrated at a scale close to the domain size. When mesoscale eddies form this energy is essentially moves downscale. And then there is the conversion of APE to KE through baroclinic instability of the initial zonal flow to further energize the mesoscale eddies. The net effect is seen to be a downscale cascade of KE. With both KE and APE cascading downscale, so does TE.

After mesoscale eddies are formed, between times 4 and 6, the first of the above processes (KE transfer from domain scale to mesoscale) has terminated and at the large scales an inverse cascade of KE is seen to be established. At these scales, the forward cascade of APE continues over this time period, leading to a net forward cascade of TE.

At wavenumbers greater than about eight, forward cascade of both KE and APE (and consequently forward cascade of TE) is seen. Recall that mesoscale shear and strain driven frontogenetic processes are most active over this time period (see Section 4.3) and explain the forward cascade of APE. Indeed, the ageostrophic secondary circulation associated with fronts and the positive feedback process mentioned in Section 4.3 are likely responsible for the forward cascade of KE seen.

In the third time period shown ($6 \leq t < 10$), in the range of scales associated with the hydrostatic geostrophic baroclinic instability, the forward cascade of APE is winding

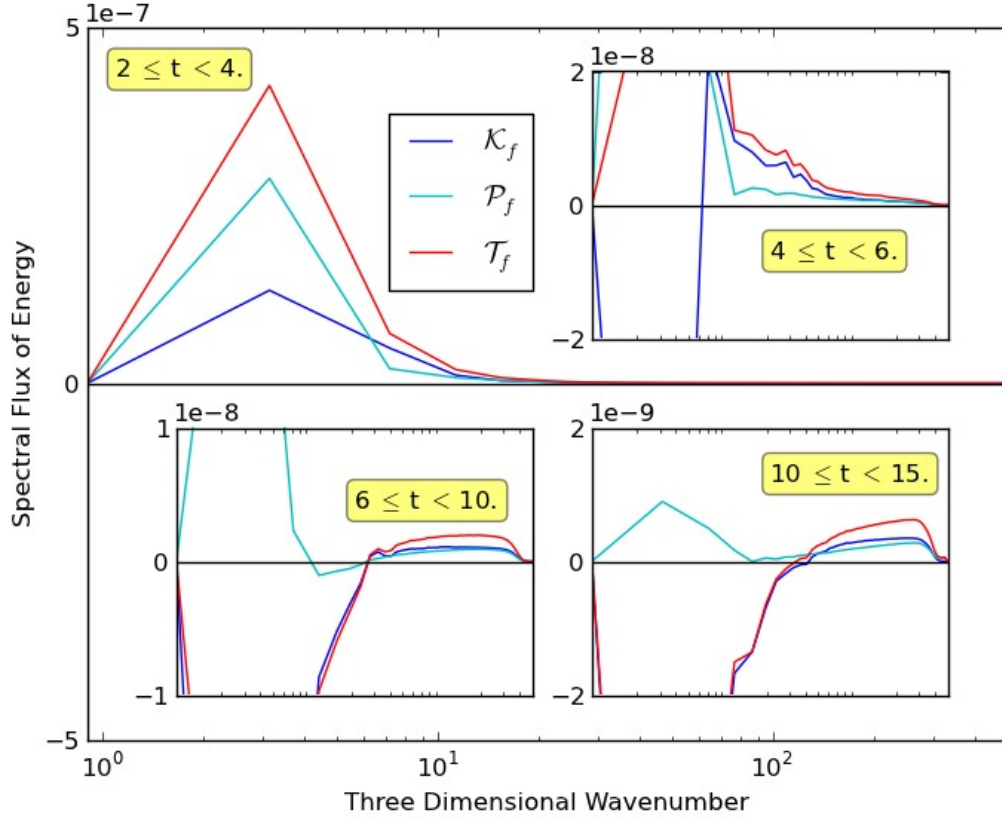


FIGURE 21. Spectral flux of kinetic (blue), available potential (cyan), and total (red) energy in the Boussinesq system with 2x resolution for the reference case ($Ro = 0.03$) averaged over four different periods

down whereas the inverse cascade of KE continues leading to an inverse cascade of TE. Over this time period, a robust forward cascade of KE, APE, and TE is seen to be established. Indeed, over this period, with frontogenetic processes winding down, while at the same time conditions for inertial and symmetric instabilities are satisfied, the forward cascade is a result of baroclinic and other instabilities that are imbalanced. Here, we note that some of these instabilities, e.g., fronts as seen earlier, can have very disparate characteristic dimensions rendering spherically averaged wavenumber a poor indicator of such characteristic scales of instability—but hopefully still useful qualitatively.

The characteristics of the spectral flux of energy over the final time period considered is seen to be similar to that in the previous time period, except that things are winding down. (Note the different scales for the y axis in the third and fourth periods.)

6.3. Nonlinear Spectral Flux of Kinetic Energy as a Function of Rossby number

Figure 22 shows the spectral flux of KE as a function of the three-dimensional wavenumber for the main sequence of Boussinesq cases considered at 2x resolution. In the main panel, this spectrum is averaged between times 6 and 10. Note that this corresponds to the third time period considered in the previous subsection and when a robust forward cascade was seen. For brevity we call this forward cascade as being caused by a set of secondary imbalanced instabilities. In the inset an average between times 4 and 6—the second time period of the previous subsection—when frontogenesis is most active

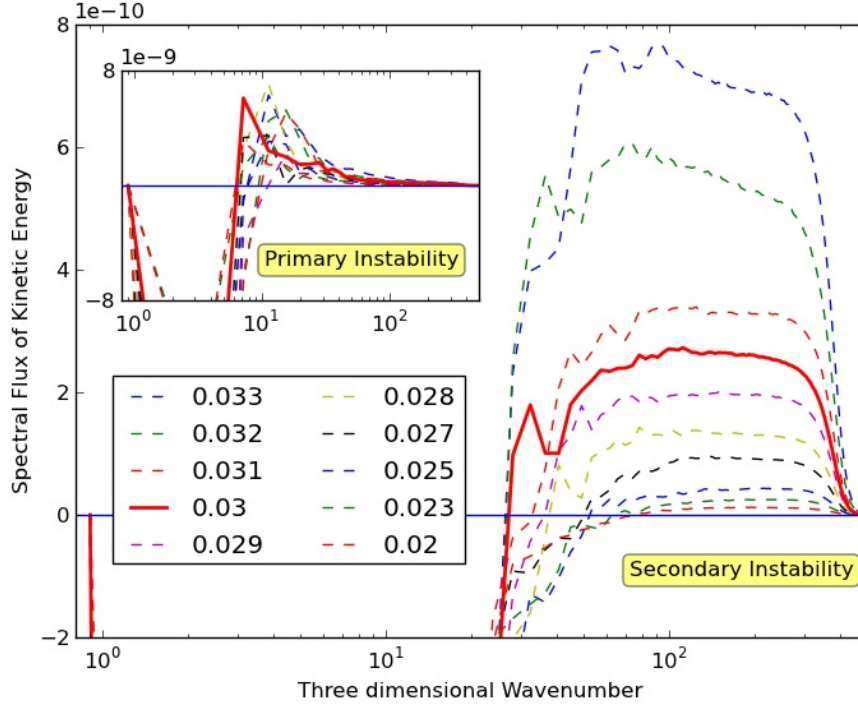


FIGURE 22. Spectral flux of energy in the Boussinesq system with $2x$ resolution. The $Ro = 0.03$ case considered in detail in previous diagnostics is shown in heavy red line; other cases with Ro ranging from 0.02 to 0.033 are shown as thinner lines. In the main panel, spectral flux of kinetic energy is plotted against the three dimensional wavenumber averaged over 13 equi-spaced snapshots between times 6 and 10, a period when dissipation is high. In the inset the average of spectral flux of kinetic energy over 6 snapshots between times 4 and 6 is plotted.

is shown. A few observations are in order here. First, the scale of the zero-crossing point of the spectral flux of KE (\mathcal{K}_f) is much smaller in the front formation phase and is likely related to the scale of the primary hydrostatic geostrophic baroclinic instability. This is also consistent with mesoscale shear and strain driving frontogenesis. The zero-crossing scale in the secondary instability phase is smaller, but the isotropic spectrum is a poor indicator of the characteristic scale of instability, as discussed earlier. A curiosity of this figure is that whereas the magnitude of the flux in the 'front formation' phase depends weakly on the Rossby number, this dependence is strong in the secondary instability phase. Indeed, since the forward cascade of kinetic energy leads in part to dissipation we expect that the dependence of the magnitude of the forward cascade flux in the main panel is exponential as well, although noisy.

Figure. 23 shows the robustness of the spectral flux of energy—a third order quantity—to changes in the coefficient of hyperviscosity and hyperdiffusivity. Here the reference simulation has been repeated two more times: In the first instance coefficients of both horizontal and vertical hyperviscosity and hyperdiffusion are increased by a factor of 2.5. In the second instance, only the coefficients of horizontal hyperviscosity and hyperdiffusion are increased by a factor of 10.

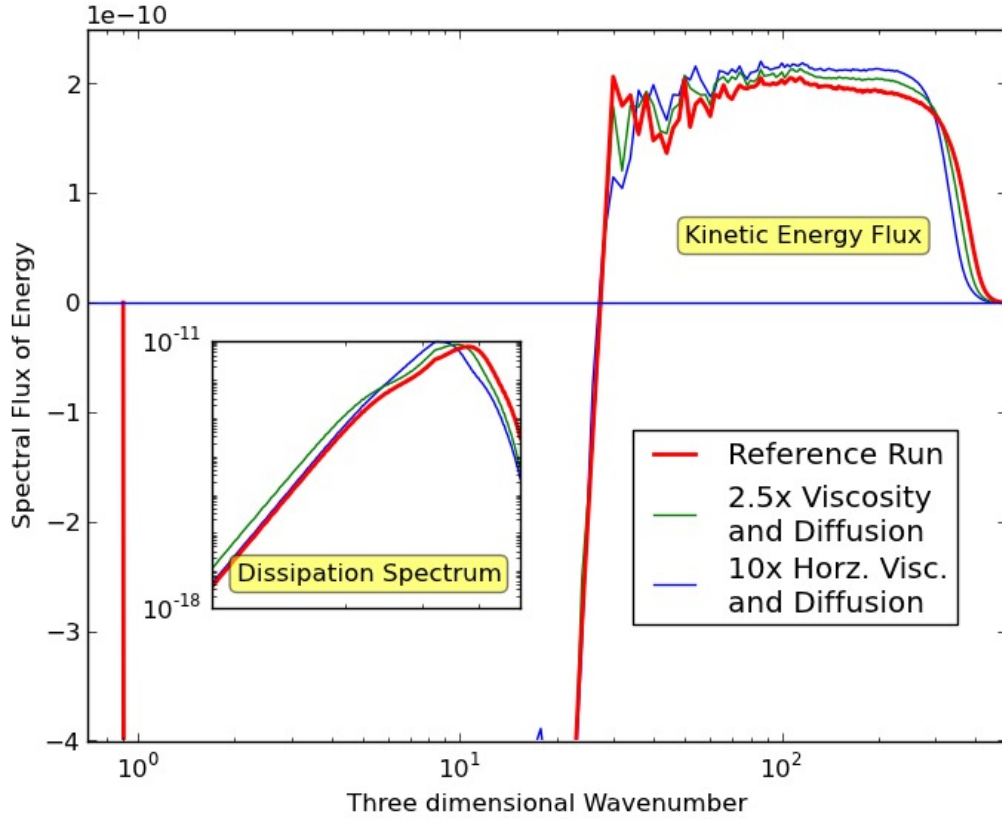


FIGURE 23. Change of spectral flux of energy and dissipation spectrum with increases in viscosity and dissipation. In addition to the reference case, two cases with increased viscosity and dissipation are shown. In the first case, coefficients of both horizontal and vertical hyperviscosity and hyperdiffusion are increased by a factor of 2.5. In the second case, only the coefficients of horizontal hyperviscosity and hyperdiffusion are increased by a factor of 10. The dependence of both the spectral flux of energy and the spectrum of dissipation is seen to be weakly dependent on the hyperviscous and hyperdiffusion coefficients.

7. Discussion and Conclusions

We consider a regime of rotating stratified flow that is of direct relevance to circulation in the oceans and in atmospheres—a regime characterized by small large-scale Rossby and Froude numbers and a small vertical to horizontal aspect ratio. In this regime, it is well established that quasi-geostrophic theory provides a good description of the *large* scales. An important consequence of the theory is a confinement of energy to large scales—scales where dissipation is ineffective. Furthermore, the steep -3 scaling of the energy spectrum due to the forward cascade of potential enstrophy predicted by quasi-geostrophic theory can be viewed as effectively precluding deviations from quasi-geostrophy. In such a regime, we consider the question of how a flow forced at large scales might equilibrate. Whereas a large body of recent research has demonstrated the importance of surface related processes in the equilibration, our interest in this article has to do with interior processes.

We use the framework of baroclinic instability—one of the main building blocks of geophysical fluid dynamics—to setup and study the problem. In this context, we note that baroclinic instability has typically been studied in three different setups (e.g., see

Vallis 2006). In the first setup—the Phillips problem—the fluid is discretized into layers in the vertical leading to discontinuous stratification and the instability is driven by interior gradients of potential vorticity. In the second setup—the Eady problem—the instability is driven by surface buoyancy gradients at two bounding horizontal surfaces. In the third setup—the Charney problem—the instability is driven by a combination of interior potential vorticity gradients and boundary buoyancy gradient at a horizontal surface. Since the interaction of energy-bearing balanced scales—oceanic mesoscale eddies—with boundaries such as the oceanic surface layer has the potential to support balanced-unbalanced energy interactions, the Eady problem or the Charney problem—in the framework of either the nonhydrostatic Boussinesq equations or the hydrostatic primitive equations—has been the preferred setup to investigate such interactions (e.g., see Molemaker *et al.* 2010; Thomas *et al.* 2008). To investigate the more direct local route of balanced-unbalanced interactions in the oceanic interior where the bulk of balanced energy resides, a setup in which baroclinic instability is driven by interior gradients of potential vorticity, as in the Phillip’s problem, is more appropriate. Furthermore, with the possibility of overturning instabilities playing a role in balanced-imbalanced interactions, a model with continuous stratification is more appropriate. To this end, we considered a setup with continuous stratification and in a periodic geometry—a setup that explicitly eliminates distinguished horizontal surfaces. This setup may be thought of as an extension of the Phillips model to one with continuous stratification, yet with no bounding horizontal surfaces, or equivalently as an extension of the Charney model to a periodic domain.

We then studied the nonlinear evolution of baroclinically unstable initial conditions that comprised of a geostrophically and hydrostatically balanced unidirectional base flow solution and a set of small perturbations, each of which was a balanced solution of the inviscid nonlinear equations. Initially energy was confined to a scale close to the size of the domain. This energy was then transferred downscale starting first with the hydrostatic geostrophic baroclinic instability. The resulting mesoscale shear and strain led to frontogenesis that then preconditioned the flow to be susceptible to unbalanced inertial and symmetric instabilities. These instabilities led to a forward cascade of energy that terminated in energy dissipation by parameterized hyperviscous and hyperdiffusive dissipation. The total dissipation over the period of the instability was less than about a tenth of a percent of the total energy and we found an exponential dependence of dissipation on Rossby number of the base flow.

As control, we carried out companion integrations or twin experiments using the quasi-geostrophic equations. A number of flow characteristics of the balanced quasi-geostrophic evolution and the evolution of the nonhydrostatic Boussinesq system were compared. There were similarities in gross characteristics of the evolution and significant differences in certain other detailed characteristics. We interpreted these differences in terms of previous theoretical analysis of instabilities. In the companion quasi-geostrophic experiments, dissipation was seen to be vanishingly small and no exponential dependence on the Rossby number of the base state was seen.

Given the fundamental nature of the dynamics involved, it is possible that the exponential scaling of dissipation with Rossby number we find will hold more generally than for the specific setup we consider. In particular, it would not be surprising if a similar scaling was realized in setups with surface layers or boundary layers. A natural question regarding this dissipation pathway, however, is as to how important it is to the energy budget of ocean circulation (e.g., Ferrari & Wunsch 2008). We recall that in the present setup, we have chosen a constant background stratification N_o^2 . On the one hand, from previous studies of geostrophic turbulence (e.g. Fu & Flierl 1980) we know that in a

more realistically stratified ocean, characteristics of the inverse cascade of energy are significantly different from that in which stratification is constant. On the other hand, recent studies such as that of Plougonven & Zeitlin (2009) show that nonlinear saturation of an imbalanced instability such as inertial instability even in a simple setting such as barotropic shear in a constantly stratified environment results in complicated vertical structure. Since dissipation would likely depend on interactions between processes such as these, estimating the importance of this energy pathway would have to depend on further numerical studies with realistic stratification and shear.

In other findings, we considered the spectrum of total energy as a function of three-dimensional wavenumber and found a break in the spectrum at small scales for the larger of the Rossby numbers considered. While the intermediate scales in the Boussinesq system and most scales in the quasi-geostrophic system scaled as k^{-3} , the small scales in the Boussinesq system for the larger of the Rossby numbers considered scaled approximately as $k^{-5/3}$. We also considered the vertical shear spectrum as a function of vertical scale and found a minimum in this spectrum at late times for the larger of Rossby numbers considered. The distribution we found is somewhat reminiscent of Fig. 1 of Gargett *et al.* (1981) which is a composite based on in-situ measurements and suggests that at late times and in the larger of the Rossby numbers considered, the simulations may be entering the regime of stratified turbulence before transitioning into a more isotropic form.

While the exponential dependence of the growth rate of unbalanced instabilities on Rossby number is well recognized (e.g., see Molemaker *et al.* 2005; Vanneste 2013, and references therein), we think that the exponential scaling of dissipation on Rossby number of the base flow we find is a further useful step in better characterizing balanced-imbalanced interactions. Indeed, to the best of our knowledge, this study is the first of its kind in this respect. We speculate that a consequence of this finding could be the introduction of a dissipative component to the parameterization of baroclinic instability: Ocean modeling has undergone vast improvements in the last half a century and one of the key improvements has been the Gent-McWilliams parameterization (Gent & McWilliams 1990) of baroclinic instability in models that do not resolve the instability scale. This parameterization consists of a skew flux that arises from an inviscid consideration of the slumping of isopycnals that is characteristic of the instability. However, preliminary analysis of simulations presented in this study suggest that a developing baroclinic instability can lead to secondary instabilities on a range of scales and that some of these instabilities can cascade energy forward to unbalanced scales. This suggests that a secondary aspect of (geostrophic hydrostatic) baroclinic instability is the ultimate dissipation of energy cascaded forward by some of the secondary instabilities—a feature that could perhaps be usefully parameterized. In keeping with advances in the representation of various unresolved processes, such a modification of the parameterization of baroclinic instability would likely result in shifting a component of dissipation represented by the (ubiquitous) homogeneous eddy viscosity to a more intermittent, process-related representation.

Investigations of spontaneous generation of imbalance is an area of extensive and ongoing research (e.g. see special collection of the *Journal of the Atmospheric Sciences* on 'Spontaneous Imbalance', May, 2009, or, e.g., (Plougonven & Snyder 2007; Danioux *et al.* 2012) for studies in the specific context of an unstable baroclinic wave). On the face of it, it may seem that the present work is not related to this area of research. This is because while the base flow we considered was an exact and balanced solution, we additionally introduced small perturbations in the initial conditions. While each of these perturbations, individually, was an exact solution as well, their superposition on the base flow rendered the initial condition to not be a solution of the nonlinear equations and further likely imbalanced. Therefore it is possible that all dissipation that ensued is traceable to

imbalance in the initial conditions. In this sense, the imbalance observed in the context of the simulations considered in this article are likely not spontaneously generated. On the other hand, it is possible these results have something to say about the nature of spontaneous generation of imbalance. To see how this may be possible, we first hypothesize that, given other things are the same, imbalance in the initial conditions considered in this article is directly proportional to the Rossby number of the base flow. If this were true (we think so), then the exponential dependence of dissipation demonstrated in this article would suggest that dissipation of balanced mesoscale energy by processes related to spontaneous generation of imbalance is likely to be negligibly small.

This research was supported by the Laboratory Directed Research and Development (LDRD) program at Los Alamos National Laboratory (project number 20110150ER). Computational resources were provided by Institutional Computing at the Los Alamos National Laboratory. Thanks to Mark Taylor both for sharing his spectral code. Brief discussions with Peter Bartello, Raf Ferrari, Patrice Klein, Jim McWilliams, Jim Riley, Shafer Smith, David Straub, Jacques Vanneste and Vladimir Zeitlin are gratefully acknowledged. Comments and suggestions by three reviewers helped improve both content and presentation.

REFERENCES

- ANDREWS, DG & HOSKINS, BJ 1978 Energy spectra predicted by semi-geostrophic theories of frontogenesis. *Journal of the Atmospheric Sciences* **35** (3), 509–512.
- BABIN, A, MAHALOV, A, NICOLAENKO, B & ZHOU, Y 1997 On the asymptotic regimes and the strongly stratified limit of rotating boussinesq equations. *Theoretical and computational fluid dynamics* **9** (3-4), 223–251.
- BARTELLO, PETER 1995 Geostrophic adjustment and inverse cascades in rotating stratified turbulence. *Journal of Atmospheric Sciences* **52**, 4410–4428.
- BOUCHUT, FRANÇOIS, RIBSTEIN, BRUNO & ZEITLIN, VLADIMIR 2011 Inertial, barotropic, and baroclinic instabilities of the bickley jet in two-layer rotating shallow water model. *Physics of Fluids* **23** (12), 126601–126601.
- BOYD, JOHN P 1992 The energy spectrum of fronts: time evolution of shocks in burgers' equation. *Journal of the Atmospheric Sciences* **49** (2), 128–139.
- CHARNEY, J. G. 1971 Geostrophic turbulence. *J. Atm. Sci.* **28**, 1087–1095.
- CHASNOV, JR 1994 Similarity states of passive scalar transport in isotropic turbulence. *Physics of Fluids* **6**, 1036–1051.
- DANIOUX, ERIC, VANNESTE, J, KLEIN, PATRICE & SASAKI, H 2012 Spontaneous inertia-gravity-wave generation by surface-intensified turbulence. *Journal of Fluid Mechanics* **699**, 153–173.
- FERRARI, RAFFAELE & WUNSCH, CARL 2008 Ocean circulation kinetic energy: Reservoirs, sources, and sinks. *Annual Review of Fluid Mechanics* **41** (1), 253.
- FRISCH, U. 1995 *Turbulence: the legacy of A. N. Kolmogorov*. Cambridge: Cambridge University Press.
- FU, LEE-LUENG & FLIERL, GLENN R 1980 Nonlinear energy and enstrophy transfers in a realistically stratified ocean. *Dynamics of Atmospheres and Oceans* **4** (4), 219–246.
- GARGETT, AEC, HENDRICKS, PJ, SANFORD, TB, OSBORN, TR & WILLIAMS, AJ 1981 A composite spectrum of vertical shear in the upper ocean. *Journal of Physical Oceanography* **11** (9), 1258–1271.
- GENT, PETER R & MCWILLIAMS, JAMES C 1990 Isopycnal mixing in ocean circulation models. *Journal of Physical Oceanography* **20** (1), 150–155.
- GILL, A. E. 1982 *Atmosphere-Ocean Dynamics*. Academic Press, New York, 662pp.
- HOLTON, J *et al.* 2004 *Dynamic meteorology*.
- HOSKINS, BJ 1974 The role of potential vorticity in symmetric stability and instability. *Quarterly Journal of the Royal Meteorological Society* **100** (425), 480–482.

- HOSKINS, BJ, DRAGHICI, I & DAVIES, HC 1978 A new look at the ω -equation. *Quarterly Journal of the Royal Meteorological Society* **104** (439), 31–38.
- LESIEUR, M. 1997 *Turbulence in Fluids*. Boston: Kluwer.
- LINDBORG, ERIK 2006 The energy cascade in a strongly stratified fluid. *Journal of Fluid Mechanics* **550**, 207–242.
- LINDZEN, RICHARD S & FOX-RABINOVITZ, MICHAEL 1989 Consistent vertical and horizontal resolution. *Monthly Weather Review* **117** (11), 2575–2583.
- MCWILLIAMS, JAMES C 1985 A uniformly valid model spanning the regimes of geostrophic and isotropic, stratified turbulence: Balanced turbulence. *Journal of the atmospheric sciences* **42** (16), 1773–1774.
- MCWILLIAMS, J. C. 2006 *Fundamentals of Geophysical Fluid Dynamics*. Cambridge, U.K.: Cambridge University Press.
- MCWILLIAMS, JAMES C, YAVNEH, IRAD, CULLEN, MICHAEL JP & GENT, PETER R 1998 The breakdown of large-scale flows in rotating, stratified fluids. *Physics of Fluids* **10**, 3178.
- MOLEMAKER, M JEROEN, MCWILLIAMS, JAMES C & CAPET, XAVIER 2010 Balanced and unbalanced routes to dissipation in an equilibrated eady flow. *Journal of Fluid Mechanics* **654**, 35.
- MOLEMAKER, M. J., MCWILLIAMS, J. C. & YAVNEH, I. 2005 Baroclinic instability and loss of balance. *J. Phys. Oceanogr.* **35**, 1505–1517.
- NADIGA, BT & STRAUB, DN 2010 Alternating zonal jets and energy fluxes in barotropic wind-driven gyres. *Ocean Modelling* **33** (3), 257–269.
- NASTROM, G.D. & GAGE, K.S. 1985 A climatology of atmospheric wavenumber spectra of wind and temperature observed by commercial aircraft. *J. Atm. Sci.* **49** (9), 950–960.
- PLOUGONVEN, RIWAL & SNYDER, CHRIS 2007 Inertia-gravity waves spontaneously generated by jets and fronts. part i: Different baroclinic life cycles. *Journal of the atmospheric sciences* **64** (7), 2502–2520.
- PLOUGONVEN, RIWAL & ZEITLIN, VLADIMIR 2009 Nonlinear development of inertial instability in a barotropic shear. *Physics of Fluids (1994-present)* **21** (10), 106601.
- RILEY, JAMES J & LINDBORG, ERIK 2008 Stratified turbulence: A possible interpretation of some geophysical turbulence measurements. *Journal of the Atmospheric Sciences* **65** (7).
- SIMON, G & NADIGA, B.T. 2014 Baroclinic instability in a triply periodic domain. *preprint*.
- SMITH, LESLIE M & WALEFFE, FABIAN 2002 Generation of slow large scales in forced rotating stratified turbulence. *Journal of Fluid Mechanics* **451**, 145–168.
- SNYDER, CHRIS, SKAMAROCK, WILLIAM C & ROTUNNO, RICHARD 1993 Frontal dynamics near and following frontal collapse. *Journal of the atmospheric sciences* **50** (18), 3194–3212.
- STRAUB, DAVID N & NADIGA, BALASUBRAMANYA T 2014 Energy fluxes in the quasigeostrophic double gyre problem. *Journal of Physical Oceanography* (2014).
- TAYLOR, MARK A, KURIEN, SUSAN & EYINK, GREGORY L 2003 Recovering isotropic statistics in turbulence simulations: The kolmogorov 4/5th law. *Physical Review E* **68** (2), 026310.
- THOMAS, LEIF N, TANDON, AMIT & MAHADEVAN, AMALA 2008 Submesoscale processes and dynamics. In *Ocean modeling in an eddying regime, Vol. 177, American Geophysical Union* (editors M.W. Hecht and H. Hasumi) pp. 17–38.
- THOMAS, LEIF N, TAYLOR, JOHN R, FERRARI, RAFFAELE & JOYCE, TERRENCE M 2013 Symmetric instability in the gulf stream. *Deep Sea Research Part II: Topical Studies in Oceanography* **91**, 96–110.
- VALLIS, G. K. 2006 *Atmospheric and Oceanic Fluid Dynamics*. Cambridge, U.K.: Cambridge University Press.
- VANNESTE, J 2013 Balance and spontaneous wave generation in geophysical flows. *Annu. Rev. Fluid Mech.* **45**, 147–172.
- VIÚDEZ, ÁLVARO & DRITSCHEL, DAVID G 2004 Optimal potential vorticity balance of geophysical flows. *Journal of Fluid Mechanics* **521** (1), 343–352.
- WAITE, MICHAEL L & BARTELO, PETER 2006 The transition from geostrophic to stratified turbulence. *Journal of Fluid Mechanics* **568**, 89–108.